



# Machine-learning based temperature- and rate-dependent plasticity model: Application to analysis of fracture experiments on DP steel

Xueyang Li, Christian C. Roth, Dirk Mohr\*

Chair of Computational Modeling of Materials in Manufacturing, Department of Mechanical and Process Engineering, ETH, Zurich, Switzerland



## ARTICLE INFO

### Keywords:

Thermo-visco-plasticity  
Hopkinson bar  
Artificial neural network  
Ductile fracture

## ABSTRACT

Slow, intermediate and high strain rate experiments are carried out on flat smooth and notched tensile specimens extracted from dual phase steel sheets. A split Hopkinson pressure bar testing system with load inversion device is utilized to achieve high strain rates. Temperature dependent experiments ranging from 20 °C to 300 °C are performed at quasi-static strain rates. The experimental results reveal a non-monotonic effect of the temperature on the stress-strain curve for DP800 steel. For the temperatures considered, the lowest and highest curves are obtained for 120 °C and 300 °C, respectively. A modified Johnson-Cook plasticity model is developed to capture the observed unconventional effect of the strain rate- and temperature on the hardening response. It includes a von Mises yield surface, a non-associated Hill'48 flow rule, a Swift-Voce reference stress-strain curve describing the rate-independent behavior at room temperature, and a neural network function depending on the plastic strain, strain rate and temperature. This model is implemented into a material user subroutine and identified using a combination of analytical formulas along with a resilient back propagation algorithm. It is found that the obtained machine-learning based Johnson-Cook plasticity model can describe all experimental data with high accuracy, including both force-displacement and local surface strain measurements. Using a hybrid experimental-numerical approach, the loading paths to fracture are determined. It is found that the temperature not only affects the plasticity of the DP800 steel in a non-monotonic manner, but also its strain to fracture, with ductility loss of up to 30% when increasing the temperature from 20 to 120 °C, followed by a gain in ductility when increasing the temperature further to 300 °C.

## 1. Introduction

The Johnson-Cook plasticity model (Johnson and Cook, 1983) is widely used in engineering practice to describe the viscoplasticity of metals. Applications include the forming of sheet metal, predicting the crashworthiness of transportation vehicles as well as the assessment of the impact response of metallic structures. The J-C-model clearly falls into the category of phenomenological models with little connection to the physical mechanisms governing the strain rate and temperature dependent response of metals. Its unmatched success over the past 30 years is mostly due to its simplicity and ease of model parameter identification. Most physics-based viscoplasticity models (e.g. Zerilli and Armstrong (1987), Follansbee and Kocks (1988), Khan and Liang (1999), Voyatzis and Abed (2005); Rusinek et al. (2007); Durrenberger et al. (2007); Abed and Makarem (2012); Kajberg and Sundin (2013); Dunand and Mohr (2017)) are based on the theory of thermally-activated dislocation motion (Conrad (1964), Kocks et al. (1975)).

\* Corresponding author.

E-mail address: [mohr@mit.edu](mailto:mohr@mit.edu) (D. Mohr).

In most physics-based viscoplasticity models, a material can deform plastically at any level of stress, while the viscosity controls the partitioning into elastic and plastic strains. In the Johnson-Cook model, a yield function defines an elastic domain in stress space, with a scalar valued deformation resistance (equating the von Mises equivalent stress) controlling its size. The central idea of the original Johnson-Cook model is to postulate that the deformation resistance may be multiplicatively decomposed into a first term depending on the equivalent plastic strain, a second term depending on the equivalent plastic strain rate, and a third term depending on the temperature. Examples for successful applications of the original Johnson-Cook model to modern engineering materials can be found in Forni et al. (2016) or Wang et al. (2017a,b).

Mostly due to recent progress in the field of ductile failure (e.g. Bai and Wierzbicki (2008), Brünig et al. (2008, 2018), Korkolis and Kyriakides (2009), Fourmeau et al. (2013), Malcher et al. (2014), Lou et al. (2014), Marcadet and Mohr (2015), Roth and Mohr (2016), Yan et al. (2016), Tancogne-Dejean et al. (2016), Liu et al. (2016), Yan et al. (2016), Lou and Yoon (2017, 2018), Baral et al. (2018), Lee et al. (2018), Chatterjee et al. (2018), Abedini et al. (2018), Lee et al. (2018), Li et al. (2018), Morin et al. (2018), Wang and Qu (2018)), there is a growing need for highly accurate predictions of the large strain plastic response of metals. As a result, so-called modified Johnson-Cook models have been developed. Sung et al. (2010) replaced the first term of the J-C model through a strain and temperature dependent function to describe the effect of moderate temperature changes during forming experiments on Advanced High Strength Steels (AHSS). Based on the results from low, intermediate and high strain rate experiments on AHSS, Roth and Mohr (2014) kept its dependency on the strain only, but they substituted the power law function of the first term through a linear combination of a Swift and Voce law. Xiao et al. (2018) substituted the first J-C term through a linear combination of Ludwik and Voce laws to model the response of aluminum 2024-T351 in Taylor impact experiments. After performing experiments on a nickel-based superalloy for strain rates of up to 400/s, Sjöberg et al. (2018) also proposed a modification of the strain hardening term of the J-C model. A similar superalloy had been subjected to ballistic loading at different temperatures by Erice et al. (2014). They found good agreement between experiments and simulations after adding a fourth multiplier to the J-C hardening model that accounts for damage.

A more substantial modification of the Johnson-Cook model has been proposed by Huh et al. (2014). In their model, the second term depends not only on the strain rate, but also on the strain. As compared to other established models, the Lim-Huh model provided the most accurate prediction of the strain rate and temperature dependent hardening response of 4340 steel and Ti6Al4V. Piao et al. (2016) also modified the third term of the J-C model by proposing a multiplier that depends on both the temperature and strain rate. In a follow-up paper, Piao et al. (2017) demonstrated the suitability of the modified Lim-Huh model for describing the response of 4340 steel, Ti6Al4V and OFHC copper in Taylor impact experiments. After analyzing their data obtained from compression experiments on a Ni-based superalloy for temperatures and strain rates ranging from 25 to 800 °C and 10<sup>-1</sup> to 10<sup>3</sup>/s, respectively, Wang et al. (2017a,b) modified the second and third J-C terms such that the resulting model captured the experimentally-observed non-monotonic temperature-dependency of the flow stress. Rahmaan et al. (2016, 2017) performed tension experiments on DP600 steel covering six orders of magnitude in strain rate (10<sup>-3</sup>–10<sup>3</sup>/s). They report that for DP600 steel, the original Johnson-Cook and Zerilli-Armstrong models were not able to accurately capture the strain hardening behavior. Inspired by the alterations proposed by Borvik et al. (2001), they modified the second J-C term by adding a power law type of expression and replaced the first term through a Voce law. A similar modified J-C model has also been used by Gruben et al. (2016) to describe the strain rate dependent stress-strain response of dual phase steel.

The particular feature of dual phase steels is that they show a strong bake hardening effect which implies that, already at temperatures between 150 and 180 °C, their properties evolve as a function of time and strain history (e.g. Ramazani et al. (2014)). They also respond to overaging which involves the tempering of the hard martensitic phase. Here, the temperature plays an important role. For example, the bainite transformation is inhibited at temperatures below 320°, while at temperatures above 300 °C, carbide particles may form leading to a decrease of tensile strength and an increase of yield strength (Kuang et al. (2016)). Gündüz and Tosun (2008) observed experimentally that the yield strength of DP600 steel increases for ageing at 100 °C, while it decreases at 200 °C due to a tempering of the martensite. In dynamic tensile testing, the duration of the experiment is related to the strain rate. Hence, the time available for thermally-activated microstructural transformations varies as a function of the strain rate. When investigating the effect of temperature and strain rate on the uniform elongation in DP600 steels, Cao et al. (2015a,b) argue that dynamic precipitation might have affected the material response at low strain rates and elevated temperatures, while the effect of martensitic transformation of the retained austenite is likely to be most pronounced at low temperatures and low strain rates.

The observed constant quest for modifying and enhancing existing temperature and rate dependent plasticity models is partially attributed to the high number of microstructural mechanisms whose activation is sensitive to the specific microstructural configuration of a polycrystalline material at hand. As an alternative to developing physics-based constitutive models, the implementation of a machine-learning based model is pursued here. In the context of mechanics, neural networks have been used as metamodeling technique for structural problems (e.g. Kohar et al. (2016, 2017)), for material parameter identification (e.g. Koh et al. (2007)) as well as for constitutive modeling (e.g. Al-Haik et al. (2006)). In the present work, the idea is to replace the second and third terms of the Johnson-Cook model through a single neural network function. Kessler et al. (2007) employed a neural network function to describe the experiments of Prasad et al. (1997) on aluminum 6061 for temperatures ranging from 300 to 550 °C and strain rates ranging from 10<sup>-3</sup> to 1/s. They used Bayesian regulation for training a neural network featuring three layers (input, hidden, output). They obtained satisfactory results with 15 and 3 neurons, respectively, for the first two layers. Another example of the successful application of a neural network function for describing the rheological response of materials has been presented by Jenab et al. (2016). In their model of anisotropic aluminum 5182-O for strain rates ranging from 0.001 to 1000/s, a neural network using 15 neurons for the input and hidden layers predicts the true stress based on the material direction, the strain rate and the current true strain.

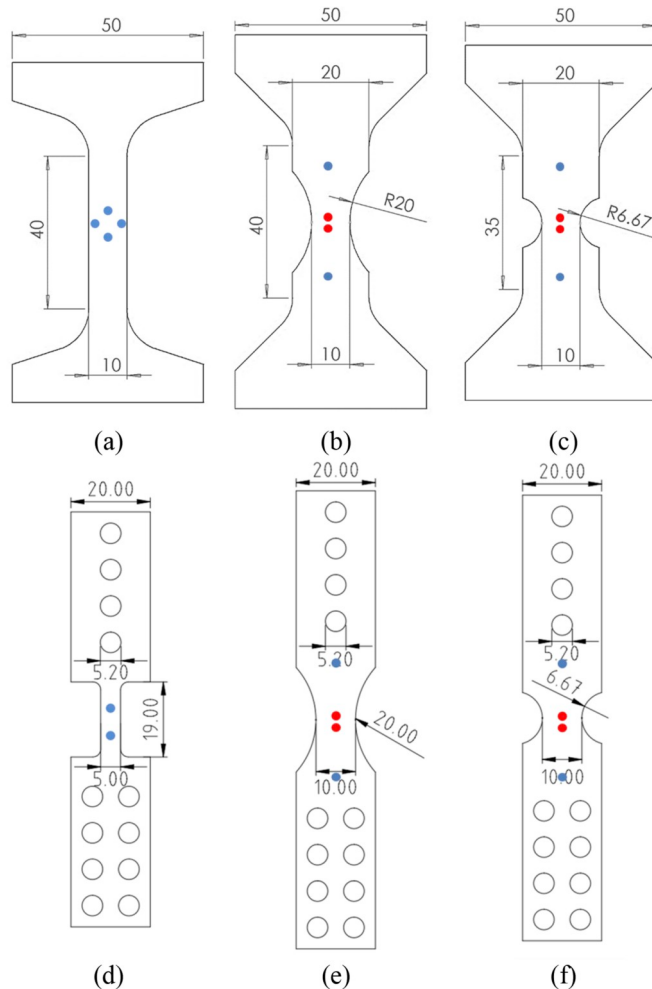


**Fig. 1.** Specimen geometries: (a) UT specimen, (b) NT20 specimen, (c) NT6 specimen, (d) D-UT specimen, (e) D-NT20 specimen, (f) D-NT6 specimen. The blue dots highlight the virtual extensometer used to measure relative displacement and speed. The red dots represent the corresponding points to measure axial surface strain. The extra pair of blue dots on the UT specimen are used to measure width strain for determination of Lankford coefficients. (For interpretation of the references to colour in this figure legend, the reader is referred to the Web version of this article.)

In the present work, low ( $0.001/\text{s}$ ), intermediate ( $\sim 1/\text{s}$ ) and high ( $\sim 1000/\text{s}$ ) strain rate experiments are performed on tension specimens extracted from DP800 steel sheets. In addition, quasi-static experiments are also performed for ambient temperatures ranging from  $20^\circ\text{C}$  to  $300^\circ\text{C}$ . Subsequently, a neural network is developed and trained based on full specimen simulations using a back-propagation scheme. For this, a user material subroutine (VUMAT for Abaqus) is developed for use in conjunction with solid elements. 3D plots are also generated showing the non-monotonic effect of the temperature on the strain hardening and the strain to fracture for the DP800 material.

## 2. Experimental procedures

### 2.1. Material and specimens

All experiments are performed on a 1.6 mm thick dual phase steel DP800. Specimens are extracted from the sheets using water-jet cutting. Drawings of the specimens for low/intermediate and high strain rate testing are shown in Fig. 1a-c and 1d-f, respectively:

- Uniaxial tension (UT) specimen featuring 40 mm long and 10 mm wide gage section. This specimen is only used for low and intermediate strain rate testing (Fig. 1a).
- Short uniaxial tension specimen (D-UT) featuring a 15 mm long and 5 mm wide gage section. The D-UT-specimens is used for high strain rate testing (Fig. 1d);
- Notched tensile specimens (NT) with symmetric circular cut-outs of radius  $R = 20\text{mm}$  (NT20, Fig. 1b) and  $R = 6.67\text{mm}$  (NT6, Fig. 1c). The maximum and minimum widths of the gage section of the NT-specimens are 20 mm and 10 mm, respectively. Note

that the gage section dimensions of the specimens used for slow, intermediate and high strain testing are identical (compare D-NT with NT drawings in Fig. 1e–f). Only the clamping area is modified in accordance with the corresponding testing device.

To facilitate digital image correlation (VIC2D, Correlated Solutions), a random black and white speckle pattern is applied to all specimens prior testing. While the pattern is spray painted for the low and intermediate strain rate experiments, airbrush with india ink is employed for the high strain rate experiments, ensuring a very flat and thin layer of paint. The average speckle size is about 80 µm.

## 2.2. Experimental technique for low strain rates

All experiments at low strain rates are conducted on a hydraulic universal testing machine (Model 8801, Instron). The specimens are clamped on their shoulders by a set of custom-made high-pressure clamps. For low strain rates, the crosshead speed is set to 2.4 mm/min for UT-specimens and 0.5 mm/min for NT-specimens. Images are acquired at a frequency of 1 Hz using a digital camera (Point Grey GS3-U3-51S5M-C with 2448 × 2048 pixels). The corresponding spatial resolution is 22 µm/pixel.

For tests at elevated temperatures, a climate chamber (Model 3119–607, Instron) is mounted on the same hydraulic testing machine. The target temperature is controlled by a thermocouple mounted on the high-pressure clamps.

## 2.3. Experimental technique for intermediate strain rates

Experiments at intermediate strain rates are carried out on the same hydraulic testing machine applying crosshead speeds of 1200 and 500 mm/min for the UT- and NT-specimens, respectively. A high-speed camera (Photron SA-Z) is employed to record images with a resolution of 1024 × 1024 pixels at a frequency of 2000 Hz, obtaining a spatial resolution of 68 µm/pixel. The image and data acquisition is triggered where the force rises, allowing for a full-synchronization of the measurements.

## 2.4. Experimental technique for high strain rates

All experiments at high strain rates are conducted on a split Hopkinson pressure bar (SHPB) system equipped with a load inversion (LID) device for tensile testing (Roth et al., 2015). The testing system features a striker bar (4990 mm long, 20 mm diameter), an input bar (5927 mm long, 20 mm diameter), a load inversion device and an output bar (5951 mm long, 20 mm diameter). All bars as well as the load inversion device are made out of steel. The incident shoulder of the specimen is mounted on the pusher using eight M5 screws, while the output shoulder is directly inserted into a slot in the output bar and fixed using four M5 screws.

Strain gages are attached on the surface of the output bar at a distance of 430 mm from the specimen/output bar interface. The data acquisition frequency for the strain gages is set to 400 kHz. The measured output bar strain history  $\varepsilon_{tra}[t]$  is used to calculate the axial force  $F_{out}[t]$  that is acting on the specimen according to

$$F_{out}[t] = E_{out} A_{out} \varepsilon_{tra}[t] \quad (1)$$

with the Young's modulus  $E_{out}$  and the area  $A_{out}$  of the bar. The images for DIC are captured with the same high speed camera as for the intermediate strain rate experiments (Photron SA-Z). The camera is positioned at a distance of about 450 mm above the specimen surface, acquiring images of 512 × 280 pixels at a frequency of 100 kHz. The spatial resolution achieved by this set-up is 70 µm/pixel.

## 3. Constitutive model

### 3.1. Yield function and non-associated flow rule

The yield function is written in terms of an equivalent stress measure,  $\bar{\sigma} = \bar{\sigma}[\sigma]$ , and a deformation resistance  $k$ ,

$$f[\sigma, k] = \bar{\sigma} - k = 0. \quad (2)$$

More specifically, the Hill'48 equivalent stress is used. Denoting the Cauchy stress vector as

$$\sigma = [\sigma_{11} \ \sigma_{22} \ \sigma_{33} \ \sigma_{12} \ \sigma_{23} \ \sigma_{13}]^T \quad (3)$$

we have

$$\bar{\sigma}[\sigma] = \sqrt{(\mathbf{P}\sigma) \cdot \sigma}. \quad (4)$$

with the symmetric matrix  $\mathbf{P}$

$$[\mathbf{P}] = \begin{bmatrix} 1 & P_{12} & -(1+P_{12}) & 0 & 0 & 0 \\ P_{12} & P_{22} & -(P_{12}+P_{22}) & 0 & 0 & 0 \\ -(1+P_{12}) & -(P_{12}+P_{22}) & 1+2P_{12}+P_{22} & 0 & 0 & 0 \\ 0 & 0 & 0 & P_{33} & 0 & 0 \\ 0 & 0 & 0 & 0 & 3 & 0 \\ 0 & 0 & 0 & 0 & 0 & 3 \end{bmatrix} \quad (5)$$

whose coefficients  $P_{12}$ ,  $P_{22}$  and  $P_{33}$  describe the anisotropy of the yield surface. The special case of an isotropic von Mises yield surface is obtained for  $P_{12} = -0.5$ ,  $P_{22} = 1$ . and  $P_{33} = 3$ .

A non-associated flow potential is introduced utilizing the Hill'48 function. In close analogy with the yield surface definition, we have

$$g[\sigma] = \sqrt{(\mathbf{G}\sigma)\cdot\sigma} \quad (6)$$

with the coefficient matrix

$$[\mathbf{G}] = \begin{bmatrix} 1 & G_{12} & -(1+G_{12}) & 0 & 0 & 0 \\ G_{12} & G_{22} & -(G_{12}+G_{22}) & 0 & 0 & 0 \\ -(1+G_{12}) & -(G_{12}+G_{22}) & 1+2G_{12}+G_{22} & 0 & 0 & 0 \\ 0 & 0 & 0 & G_{33} & 0 & 0 \\ 0 & 0 & 0 & 0 & 3 & 0 \\ 0 & 0 & 0 & 0 & 0 & 3 \end{bmatrix} \quad (7)$$

An associated flow rule is recovered when setting  $\mathbf{G} = \mathbf{P}$ .

The increment in the plastic strain vector  $\varepsilon_p$  is denoted as:

$$d\varepsilon_p = d\lambda \frac{\partial g[\sigma]}{\partial \sigma} \quad (8)$$

$$\varepsilon_p = \left[ \varepsilon_{11}^p \ \varepsilon_{22}^p \ \varepsilon_{33}^p \ 2\varepsilon_{12}^p \ 2\varepsilon_{23}^p \ 2\varepsilon_{13}^p \right]^T \quad (9)$$

The equivalent plastic strain rate is defined as the work-conjugate to the equivalent stress,

$$\sigma: \dot{\varepsilon}^p = \bar{\sigma} \dot{\varepsilon}_p \quad (10)$$

The evolution of the equivalent plastic strain as a function of the plastic multiplier then reads

$$d\bar{\varepsilon}_p = d\lambda \frac{g}{\bar{\sigma}} \quad (11)$$

### 3.2. Decomposition of deformation resistance

The deformation resistance is multiplicatively decomposed into a reference hardening function and a neural network function that describes the strain rate and temperature dependent behavior. The yield function reads as

$$f[\sigma, \bar{\varepsilon}_p, \dot{\varepsilon}_p, T] = \bar{\sigma}[\sigma] - k[\bar{\varepsilon}_p, \dot{\varepsilon}_p, T] = 0, \quad (12)$$

with the deformation resistance given by the modified Johnson-Cook law,

$$k[\bar{\varepsilon}_p, \dot{\varepsilon}_p, T] = k_{SV}[\bar{\varepsilon}_p]k_{NN}[\bar{\varepsilon}_p, \dot{\varepsilon}_p, T] \quad (13)$$

#### 3.2.1. Reference hardening function

The isotropic strain hardening term  $k_{SV}[\bar{\varepsilon}_p]$  is represented by a linear combination of power and exponential law,

$$k_{SV}[\bar{\varepsilon}_p] = \alpha k_S[\bar{\varepsilon}_p] + (1-\alpha)k_V[\bar{\varepsilon}_p] \quad (14)$$

with the power law ([Swift \(1952\)](#)),

$$k_S[\bar{\varepsilon}_p] = A(\varepsilon_0 + \bar{\varepsilon}_p)^n, \quad (15)$$

and the exponential law ([Voce \(1948\)](#)),

$$k_V[\bar{\varepsilon}_p] = k_0 + Q(1 - e^{-\beta\bar{\varepsilon}_p}) \quad (16)$$

In sum, this parametric form features the Swift parameters  $\{A, \varepsilon_0, n\}$ , the Voce parameters  $\{k_0, Q, \beta\}$ , and the weighting parameter  $\alpha \in [0,1]$ .

#### 3.2.2. Neural network function accounting for effects of strain rate and temperature

A feed-forward neural network is introduced to represent the function  $k_{NN}[\bar{\varepsilon}_p, \dot{\varepsilon}_p, T]$  which describes the effects of the strain, strain rate and temperature. For an N-dimensional vector  $\mathbf{x}$  of input variables, the scalar output variable  $k_{NN}$  of the neural network is computed as follows:

1. Normalization of all input variables by projecting them onto the interval  $[-1, +1]$ . This is used to avoid any bias caused by differences of scale between the various entries of the input vector (strains and temperatures, for instance) during the first few iterations of optimization. For  $i = 1, \dots, N$ , we write

$$\bar{x}_i = \text{norm}[x_i] = -1 + 2 \frac{x_i - a_i}{b_i - a_i} \quad (17)$$

with the model parameters  $a_i \leq \min(x_i)$  and  $b_i \geq \max(x_i)$ . The allowable range for the input of our neural network based function is defined by the interval  $[a_i, b_i]$  from which the input variables are projected onto the normalized interval  $[-1, +1]$ . The normalized input variables  $\bar{x}_i$  are then assigned to their corresponding neurons in the input layer vector

$$\mathbf{H}^{(0)} = [\bar{x}_1, \dots, \bar{x}_N]^T. \quad (18)$$

2. Activation of the first of the  $M$  hidden layers, represented by the  $P$ -dimensional vector  $\mathbf{H}^{(1)}$ . For the first hidden layer, we choose a wider layer with more neurons as compared to the input layer (domain expansion with  $P \geq N$ ) to prevent information loss (Tamura and Tateishi (1997), Huang (2003)). For  $i = 1, \dots, P$ , we have

$$H_i^{(1)} = \tanh \left[ \sum_{j=1}^N W_{ij}^{(0)} H_j^{(0)} + b_i^{(0)} \right] \quad (19)$$

with  $\mathbf{W}^{(0)}$  and  $\mathbf{b}^{(0)}$  representing the weight matrix and bias vector, respectively. The bias vector adds a constant term to each neuron, which enhances the fitting capability of the network. In practice, the bias vector is implemented by adding a bias node (neuron) with constant activation of 1 in the previous layer. The bias vector is then incorporated into the weight matrix by adding one extra column to  $\mathbf{W}^{(0)}$  with the same values as the bias vector (Ben-David and Shalev-Shwartz, 2014). A hyperbolic tangent is chosen as the activation function, and hence its derivative reads

$$\frac{\partial}{\partial x} \tanh(x) = 1 - \tanh^2(x). \quad (20)$$

3. Computation of the subsequent  $M - 1$  hidden layers, as represented by the  $P$ -dimensional vectors  $\mathbf{H}^{(k)}$ , with  $k = 2, \dots, M$  denoting the layer number.

For  $i = 1, \dots, P$ , we obtain

$$H_i^{(k)} = \tanh \left[ \sum_{j=1}^P W_{ij}^{(k-1)} H_j^{(k-1)} + b_i^{(k-1)} \right] \quad (21)$$

4. Computation of the output layer from the  $M^{\text{th}}$  (last) hidden layer. In this study, the neural network, the output layer  $\bar{y}$  is a scalar,

$$\bar{y} = \tanh \left[ \sum_{l=1}^P W_l^{(M)} H_l^{(M)} + b^{(M)} \right]. \quad (22)$$

The scalar output variable  $k_{NN}$  then is the projection of the output layer  $\bar{y}$  from  $[-1, +1]$  to the design space through linear scaling

$$k_{NN} = c_{out} + \frac{1}{2}(d_{out} - c_{out})(\bar{y} + 1) \quad (23)$$

with interval  $[c_{out}, d_{out}]$  corresponding to the designed output space of our neural network function.

### 3.3. Temperature evolution

Following the model presented by Roth and Mohr (2014), the temperature is treated as internal state variable and determined through the evolution equation

$$dT = \omega[\dot{\varepsilon}_p] \frac{\eta_k}{\rho C_p} \bar{\sigma} d\bar{\varepsilon}_p, \quad (24)$$

where  $\eta_k$  denotes the Taylor-Quinney coefficient,  $\rho$  is the density and  $C_p$  is the specific heat capacity of the material.  $\omega[\dot{\varepsilon}_p]$  is a monotonic function of the strain rate that changes the thermal conditions from isothermal ( $\omega = 0$ ) to adiabatic conditions ( $\omega = 1$ ):

$$\omega[\dot{\varepsilon}_p] = \begin{cases} 0 & \text{for } \dot{\varepsilon}_p < \dot{\varepsilon}_{it} \\ \frac{(\dot{\varepsilon}_p - \dot{\varepsilon}_{it})^2(3\dot{\varepsilon}_a - 2\dot{\varepsilon}_p - \dot{\varepsilon}_{it})}{(\dot{\varepsilon}_a - \dot{\varepsilon}_{it})^3} & \text{for } \dot{\varepsilon}_{it} \leq \dot{\varepsilon}_p \leq \dot{\varepsilon}_a \\ 1 & \text{for } \dot{\varepsilon}_a < \dot{\varepsilon}_p \end{cases} \quad (25)$$

with the model parameters  $\dot{\varepsilon}_{it}$  and  $\dot{\varepsilon}_a$  (isothermal and adiabatic limit strain rates). As an alternative to using Eqs. (24) and (25), the temperature could also be computed through full thermo-mechanical analysis, which is recommended when dealing with sheet metal forming operations (that include heat transfer between work-piece and tool). Since the neural network model makes use of the temperature as input variable, there is no need to recalibrate the model when using full thermo-mechanical analysis.

**Table 1**

DP800 material properties determined from tensile tests: yield stress  $\sigma_{YS}$ , the ultimate tensile strength  $\sigma_{UTS}$ , the engineering strains at ultimate tensile strength  $\varepsilon_U$ , the engineering strain to fracture  $\varepsilon_T$  and Lankford ratios  $r_\alpha$ .

$\alpha [^\circ]$	$\sigma_{YS} [\text{MPa}]$	$\sigma_{UTS} [\text{MPa}]$	$\varepsilon_U [-]$	$\varepsilon_T [-]$	$r_\alpha [-]$
0	651	785	0.11	0.36	0.78
45	652	780	0.11	0.38	1.06
90	670	799	0.11	0.34	0.90

### 3.4. Material model parameter identification

The plasticity model parameters are identified as follows:

- The parameters for anisotropic flow potential are derived from the Lankford ratios measured from uniaxial tensile experiments with 9 mm long virtual extensometers on both axial and width direction (Fig. 1a).

$$G_{12} = -\frac{r_0}{1+r_0}, \quad G_{22} = \frac{r_0}{r_90} \frac{1+r_90}{r_0}, \quad G_{33} = \frac{1+2r_{45}}{r_90} \frac{r_0+r_90}{1+r_0} \quad (26)$$

- The Swift and Voce strain hardening parameters are identified with least-square fit of the true stress-plastic strain curves from uniaxial tensile tests at  $\dot{\varepsilon} = \dot{\varepsilon}_{it} = 0.001/\text{s}$  up to the onset of necking obtained from 30 mm long virtual extensometers.
- The parameter  $\alpha$  of the mixed Swift-Voce hardening law is identified through inverse analysis of room temperature, low strain rate NT20 experiments.
- The parameters  $\{E, \nu, \rho, \eta_k, \dot{\varepsilon}_a\}$  are taken from literature (see Table 3).
- The specific heat  $C_p$  at room temperature is experimentally determined using differential scanning calorimetry (Mettler Toledo DSC 1).

The neural network function describing the effects of temperature and strain rate is identified through a machine learning approach as described in the following section.

## 4. Machine learning

### 4.1. Basic procedure

The parameters defining the feed forward neural network are identified through supervised learning using a resilient back-propagation algorithm (Riedmiller and Braun, 1993). The fundamental principle of backpropagation is the repeated utilization of the chain rule to calculate the partial derivatives of the cost function  $Cost$  with respect to the weights  $W_{ij}^{(k)}$ ,

$$\frac{\partial Cost}{\partial W_{ij}^{(k)}} = \frac{\partial Cost}{\partial k_{NN}} \frac{\partial k_{NN}}{\partial W_{ij}^{(k)}}, \quad (27)$$

where  $k_{NN}$  represents the network output and  $k$  denotes the layer number. The specific choice of the cost function comparing the experimental and numerical results will be discussed in the next subsection. The detailed steps to calculate the gradient of cost function with respect to network parameters can be found in Rumelhart et al. (1986) and Ben-David and Shalev-Shwartz (2014). Once the partial derivative with respect to the weights is known, the cost function is minimized through a gradient descent scheme, i.e. for each iteration, a step is taken in the direction of the negative of the gradient to improve the solution. Here,  $\Delta W_{ij}^{(k)}$  denotes the change in weight, which is calculated by multiplying the negative of the gradient with the so-called learning rate  $\eta_L$ ,

**Table 2**

Plasticity model parameters for DP800.

$E [\text{MPa}]$	$\nu [-]$	$\rho [\text{kg/m}^3]$	$A [\text{MPa}]$	$\varepsilon_0 [-]$	$n [-]$	$k_0 [\text{MPa}]$
210	0.3	7850	1149.00	6.29E-5	0.114	593.21
$Q [\text{MPa}]$	$\beta [-]$	$\alpha [-]$	$\eta_k [-]$	$\dot{\varepsilon}_{it} [\text{1/s}]$	$\dot{\varepsilon}_a [\text{1/s}]$	$C_p [\text{J/kgK}]$
181.53	27.01	0.70	0.9	0.001	1.379	624
$G_{12}$	$G_{22}$	$G_{33}$	$P_{12}$	$P_{22}$	$P_{33}$	
-0.43	0.93	3.27	-0.48	0.95	3.01	

**Table 3**

Reference pseudo dataset, NT20, room temperature low strain rate test.

Input	$\bar{\varepsilon}_p$	0	0.01	0.02	0.03	...	1
	$\dot{\varepsilon}_p$	$10^{-3}$	$10^{-3}$	$10^{-3}$	$10^{-3}$	...	$10^{-3}$
	T	293	293	293	293	...	293
Target	$k_{NN}$	1.0	1.0	1.0	1.0	...	1.0

$$\Delta W_{ij}^{(k)} = -\eta_L \frac{\partial \text{Cost}}{\partial W_{ij}^{(k)}}. \quad (28)$$

Using resilient propagation allows the weight update to be solely dependent on the direction, instead of the value of the gradient. For the first iteration, the size of the weight update is calculated as

$$\Delta_{ij}^{(1)} = \left| -\eta_L \frac{\partial \text{Cost}}{\partial W_{ij}^{(k)}} \right|. \quad (29)$$

For the subsequent iterations  $t$ , the size of the weight update is evaluated based on the current gradient direction compared to the previous one

$$\Delta_{ij}^{(t)} = \begin{cases} |\eta^+ (\Delta W_{ij}^{(k)})^{(t-1)}|, & \text{if } \left( \frac{\partial \text{Cost}}{\partial W_{ij}^{(k)}} \right)^{(t-1)} * \left( \frac{\partial \text{Cost}}{\partial W_{ij}^{(k)}} \right)^{(t)} > 0 \\ |\eta^- (\Delta W_{ij}^{(k)})^{(t-1)}|, & \text{if } \left( \frac{\partial \text{Cost}}{\partial W_{ij}^{(k)}} \right)^{(t-1)} * \left( \frac{\partial \text{Cost}}{\partial W_{ij}^{(k)}} \right)^{(t)} < 0 \\ |(\Delta W_{ij}^{(k)})^{(t-1)}|, & \text{else} \end{cases}. \quad (30)$$

Limited through  $0 < \eta^- < 1 < \eta^+$ ,  $\eta^-$  denotes a factor that reduces the weight update whenever the derivative changes its sign, often indicating a jump over a local minimum. In contrast,  $\eta^+$  is the increase factor that amplifies the weight update whenever the derivative retains its sign in shallow regions. The size of the weight update is then capped between a maximum  $\Delta_{\max}$  and minimum  $\Delta_{\min}$  to achieve a smoothed behavior of the error decrease.

$$\Delta_{ij}^{(t)} = \max(\Delta_{ij}^{(t)}, \Delta_{\min}) \quad (31)$$

$$\Delta_{ij}^{(t)} = \min(\Delta_{ij}^{(t)}, \Delta_{\max}) \quad (32)$$

In addition to resilient gradient descent, a momentum term that scales the influence of previous iteration to current is added to stabilize the convergence and to allow for acceleration during shallow regions:

$$(\Delta W_{ij}^{(k)})^{(t)} = -\text{sgn}\left(\frac{\partial \text{Cost}}{\partial W_{ij}^{(k)}}\right)^{(t)} * \Delta_{ij}^{(t)} + \mu_M (\Delta W_{ij}^{(k)})^{(t-1)} \quad (33)$$

with  $\mu_M$  representing the momentum parameter.

The training of neural networks utilizing gradient descent algorithms is usually conducted in a so-called batch or online manner (Wilson and Martinez, 2003). We apply a batch training approach to utilize its advantage in parallel execution of finite element simulations on multiple CPUs. For such regression type of task with a small training dataset, the difference in accuracy between the models trained through online and batch training is expected to be negligibly small. For an ordinary batch training approach, the update in the weight matrices is performed once  $u_{batch}$  instances of a training sample have been evaluated. A full schematic of the machine learning procedure is shown in Fig. 2. It includes a pre-training and a final training sequence which are described in the sequel.

#### 4.2. Stage I: pre-training

The experimental data from notched tension experiments comes in the form of force-displacement curves, i.e. the stress-strain response of the material is not directly available. To obtain the stress-strain response of the material at high strains, we implement an inverse procedure, which requires the execution of a non-linear finite element analysis for each set of network parameters (Roth and Mohr, 2014).

To accelerate the training procedure, a pseudo dataset is created for the initial pre-training stage, as shown in Tables 3–5. It comprises entries of the equivalent plastic strain, equivalent plastic strain rate and temperature at different loading speeds and temperatures. The target of this pseudo dataset corresponds to a first user estimate of the multiplier  $k_{NN}$  based on the force-displacement curves for different temperatures and strain rates. It is worth noting that pre-training with a pseudo dataset is not necessary, yet recommended as it provides a beneficial starting point for the optimization with a smoothed hardening model suitable

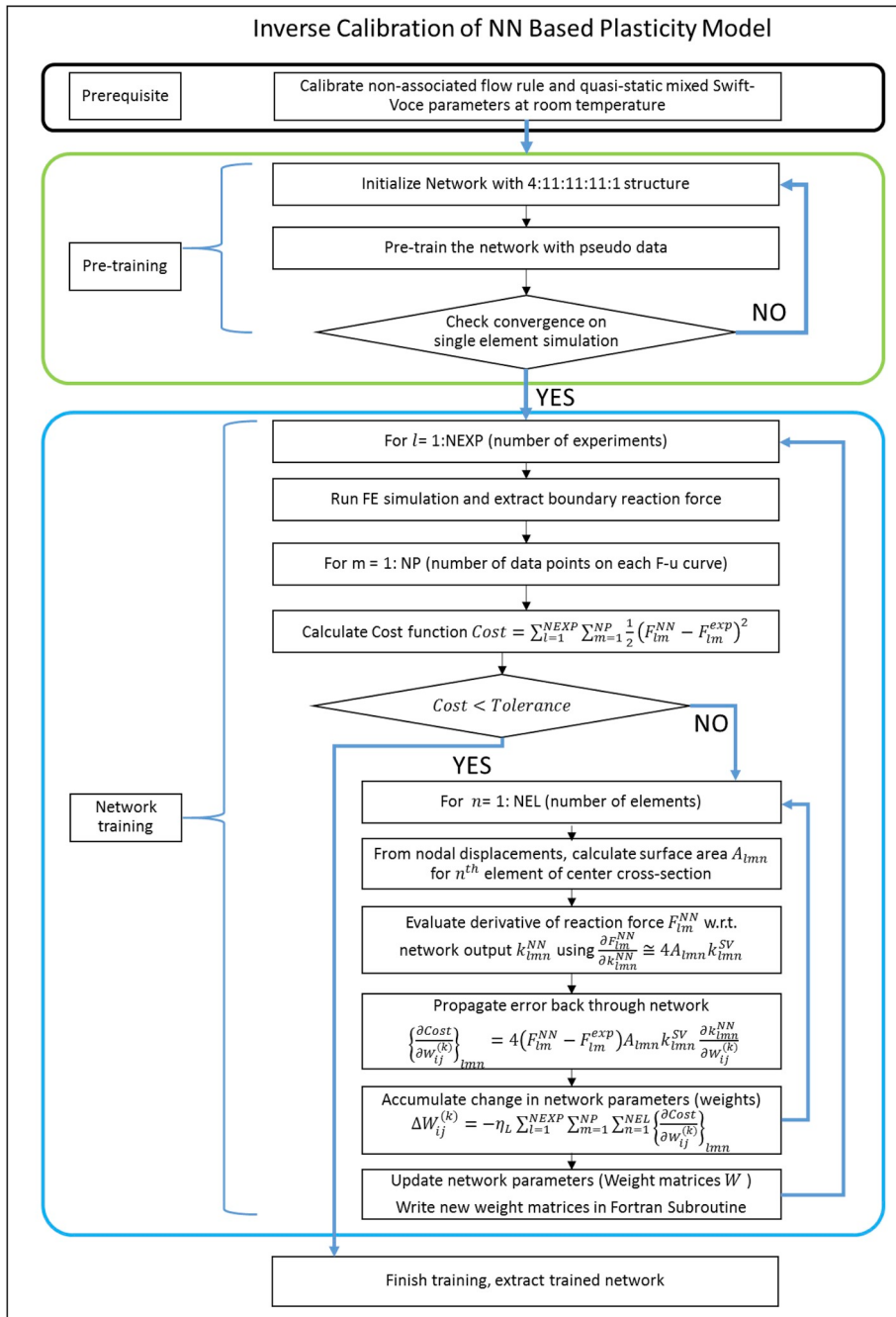


**Fig. 2.** Schematic diagram for neural network parameter identification.

**Table 4**

Pseudo dataset for NT20, high strain rate experiment.

Input	$\bar{\varepsilon}_p$	0	0.01	0.02	0.03	...	1
	$\dot{\bar{\varepsilon}}_p$	$10^3$	$10^3$	$10^3$	$10^3$	...	$10^3$
	T	293	293	293	293	...	293
Target	$k_{NN}$	1.2	1.2	1.2	1.2	...	1.2

**Table 5**

Pseudo dataset for NT20, high temperature experiment.

Input	$\bar{\varepsilon}_p$	0	0.01	0.02	0.03	...	1
	$\dot{\varepsilon}_p$	$10^{-3}$	$10^{-3}$	$10^{-3}$	$10^{-3}$	...	$10^{-3}$
	$T$	573	573	573	573	...	573
Target	$k_{NN}$	1.05	1.05	1.05	1.05	...	1.05

for finite element analysis.

The actual network training begins with the initialization of the network parameters. This involves setting all nodal activations values to zero, except for the bias nodes, which are set to 1. The entries of the weight matrices are randomly initialized between  $[-1, +1]$ ,

$$W_{ij}^{(k)} = \text{rand}(-1, 1). \quad (34)$$

The network  $k_{NN}$  is then trained using the resilient back-propagation method with the created pseudo dataset. Here, the cost function  $C_{MSE}$  can be directly formulated in terms of the network output,

$$C_{MSE} = \frac{1}{2}(k_{NN} - k_T)^2 \quad (35)$$

where  $k_T$  is the target and  $k_{NN}$  is the network output. The corresponding gradient of the residual with respect to the network output then reads,

$$\frac{\partial C_{MSE}}{\partial k_{NN}} = (k_{NN} - k_T) \quad (36)$$

#### 4.3. Stage II: final training

The final training stage involves repeated finite element simulations of notched tension experiments. The cost function is defined through the differences between the predicted and experimentally-measured forces. Formally, we write

$$Cost = \sum_{l=1}^{NEXP} \sum_{m=1}^{NP} \frac{1}{2} (F_{lm}^{NN} - F_{lm}^{\exp})^2 \quad (37)$$

with  $F_{lm}^{NN}$  and  $F_{lm}^{\exp}$  denoting the respective predicted and measured forces. The index  $l$  denotes the experiment number ( $l = 1, \dots, NEXP$ ), and the index  $m$  denotes the data point number after discretizing each curve though a total of  $NP$  data points (evenly spaced on the displacement axis).

Throughout the training, the weights  $W_{ij}^{(k)}$  (with  $k$  denoting the layer number,  $i$  denoting the neuron number of the  $(k+1)^{\text{th}}$  layer, and  $j$  denoting the neuron number of the  $k^{\text{th}}$  layer, see Section 3.3.2) are updated according to the learning rule

$$\{W_{ij}^{(k)}\}_{\text{new}} = \{W_{ij}^{(k)}\}_{\text{old}} - \eta_L \frac{\partial Cost}{\partial W_{ij}^{(k)}} \quad (38)$$

with the scalar multiplier  $\eta_L \in (0, 1]$  (learning rate). The computation of the partial derivatives  $\partial Cost / \partial W_{ij}^{(k)}$  is particularly challenging when dealing with results from finite element simulations. The problem is that, in case of specimens with heterogeneous mechanical fields, the incremental stress-strain response of each element is affected in a different manner when changing the weights of the neural network function  $k^{NN} = k^{NN}(\bar{\varepsilon}_p, \dot{\varepsilon}_p, T, W_{ij}^{(k)})$ , while the cost function is written in terms of an integral expression (total force). According to the chain rule, we have

$$\frac{\partial Cost}{\partial W_{ij}^{(k)}} = \sum_{l=1}^{NEXP} \sum_{m=1}^{NP} \left[ (F_{lm}^{NN} - F_{lm}^{\exp}) \sum_{n=1}^{NEL} \left( \frac{\partial F_{lm}^{NN}}{\partial k_{lmn}^{NN}} \frac{\partial k_{lmn}^{NN}}{\partial W_{ij}^{(k)}} \right) \right] \quad (39)$$

with the index  $n$  numbering the  $NEL$  elements comprised in the narrowest cross-section of the specimen gage section (elements highlighted in Fig. 3). Provided that the network inputs (strain, strain rate and temperature) are known for the element  $n$ , it is straightforward to compute the corresponding partial derivatives  $\partial k_{lmn}^{NN} / \partial W_{ij}^{(k)}$  at any instant  $m$ , and for any experiment  $l$ . We therefore focus on the computation of the partial derivative  $\partial F_{lm}^{NN} / \partial k_{lmn}^{NN}$ . Assuming a linear variation of the axial stress over the current cross-sectional area  $A_{lmn}$  of each element, the total axial force reads

$$F_{lm}^{NN} = 4 \sum_{n=1}^{NEL} A_{lmn} \sigma_{lmn} \quad (40)$$

with  $\sigma_{lmn}$  denoting the axial Cauchy stress at the Gauss point of the element  $l$  (first-order solid element with reduced integration) at time  $m$ , for the experiment  $n$ , and the factor four being due to the symmetry of the FE model. The partial derivative  $\partial F_{lm}^{NN} / \partial k_{lmn}^{NN}$  then

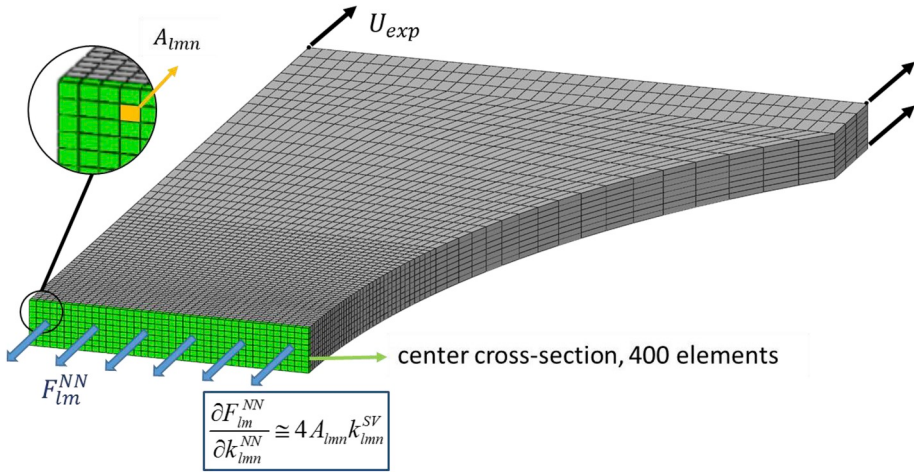


**Fig. 3.** Finite element model of NT20 specimen. Only one eighth of specimen is modeled due to symmetry. There are eight elements through the thickness of half of the specimen and 400 elements within the center cross-section (green area). (For interpretation of the references to colour in this figure legend, the reader is referred to the Web version of this article.)

reads

$$\frac{\partial F_{lm}^{NN}}{\partial k_{lmn}^{NN}} = 4A_{lmn} \frac{\partial \sigma_{lmn}}{\partial k_{lmn}^{NN}} = 4A_{lmn} \frac{\partial \sigma_{lmn}}{\partial \bar{\sigma}_{lmn}} \frac{\partial \bar{\sigma}_{lmn}}{\partial k_{lmn}^{NN}} \quad (41)$$

where we distinguish between the axial stress  $\sigma_{lmn}$  and the equivalent stress  $\bar{\sigma}_{lmn}$ . In the NT20 specimens, the stress state is close to uniaxial tension at the gage section center. Hence, we have  $\sigma_{lmn} \approx \bar{\sigma}_{lmn}$  and  $\partial \sigma_{lmn} / \partial \bar{\sigma}_{lmn} \approx 1$ . Furthermore, assuming that all elements deform plastically at the instant  $m$ , we have  $\bar{\sigma}_{lmn} = k_{lmn}^{SV} k_{lmn}^{NN}$  and thus  $\partial \bar{\sigma}_{lmn} / \partial k_{lmn}^{NN} = k_{lmn}^{SV}$ . A simplified expression for Eq. (41) then reads

$$\frac{\partial F_{lm}^{NN}}{\partial k_{lmn}^{NN}} \approx 4A_{lmn} k_{lmn}^{SV}. \quad (42)$$

Using Eq. (42) in Eq. (39), then yields

$$\frac{\partial \text{Cost}}{\partial W_{ij}^{(k)}} = 4 \sum_{l=1}^{NEXP} \sum_{m=1}^{NP} \left[ (F_{lm}^{NN} - F_{lm}^{EXP}) \sum_{n=1}^{NEL} A_{lmn} k_{lmn}^{SV} \frac{\partial k_{lmn}^{NN}}{\partial W_{ij}^{(k)}} \right] \quad (43)$$

which can be readily evaluated based on the following FE outputs at instant  $m$  from the simulation of experiment  $l$  with the material model defined through the weights  $\{W_{ij}^{(k)}\}_{old}$ :

- total axial force  $F_{lm}^{NN}$ ;
- current cross-sectional areas  $A_{lmn}$ , the equivalent plastic strain  $\bar{\epsilon}_{lmn}^p$ , the equivalent plastic strain rate  $\dot{\bar{\epsilon}}_{lmn}^p$ , and the temperature  $T_{lmn}$  for all elements  $n = 1, \dots, NEL$  comprised in the narrowest specimen cross-section);

Note that  $k_{lmn}^{SV} = k^{SV}(\bar{\epsilon}_{lmn}^p)$  is obtained from Eq. (14), while  $\partial k_{lmn}^{NN} / \partial W_{ij}^{(k)}$  is obtained from executing a standard back propagation algorithm with the network inputs  $\bar{\epsilon}_{lmn}^p$ ,  $\dot{\bar{\epsilon}}_{lmn}^p$  and  $T_{lmn}$ .

In the present work, the final training is performed using  $NP = 200$ ,  $NEL = 400$  and  $NEXP = 8$ . The training is complete once the total error is lower than a set threshold or once a maximum number of iterations is reached.

## 5. Results and discussion

### 5.1. Experimental results

#### 5.1.1. Experiments at room temperature

The true stress-strain curves are extracted from UT-experiments for loading along the 0°-, 45°- and 90°-directions. In case of the UT specimens, the experimental data is only exploited up to the point of maximum force. The obtained stress-strain curves (Fig. 4a) are almost identical for loading along the 0°- and 45°-directions, while the stress is about 2% higher for the 90°-direction. It is interesting to observe a short Lüders' plateau at the onset of yielding (which is rather unusual for dual phase steel, but as pointed out by Hüper et al. (1999), the Lüders elongation is a function of the hard phase volume fraction within the ferrite matrix; Ramazani et al. (2016) suggest that Lüders bands in DP steels are caused by a Cottrell effect). After calculating the thickness strain assuming plastic incompressibility, the Lankford ratios  $r_0 = 0.78$ ,  $r_{45} = 1.06$  and  $r_{90} = 0.90$  are determined from the UT experiments. They are also

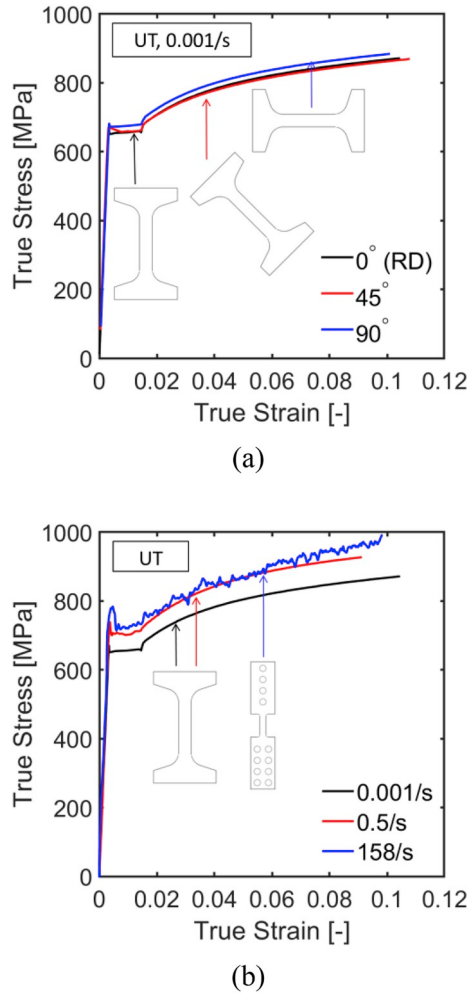


**Fig. 4.** (a) True stress – true strain curves as obtained from quasi-static uniaxial tension experiments at 0.001/s for 0°, 45° and 90° with respect to rolling direction. (b) True stress – true strain curves for low, intermediate and high strain rate experiments along the rolling direction. Note the positive strain rate hardening.

summarized in Table 1 along with the yield stress  $\sigma_{YS}$ , the ultimate tensile strength  $\sigma_{UTS}$ , the engineering strains at ultimate tensile strength  $\varepsilon_U$ , and the engineering strain to fracture  $\varepsilon_T$ . Due to excellent repeatability, only one representative curve is shown per experiment. The results from uniaxial tension experiments (along the rolling direction) at different strain rates (Fig. 4b) reveal a positive strain rate effect in the yield stress. It increases by about 7% when increasing the strain rate from  $10^{-3}/\text{s}$  to  $\sim 1/\text{s}$ , while a minor additional increase of about 3% is observed when increasing the strain rate from  $\sim 1/\text{s}$  to  $\sim 10^2/\text{s}$ .

Fig. 5 shows the force-displacement curves for tension experiments on NT6 and NT20 specimens for three different loading velocities. All curves are plotted up to the point where the axial force drops abruptly. In each NT experiment, a force maximum is observed well before fracture occurs. Note that after the force maximum, the decrease in axial force per applied displacement increment is higher for faster loading speeds. For the fast NT6 experiment, the force maximum occurs at a displacement of 0.59 mm, which is 0.02 mm earlier than for the intermediate, and 0.04 mm earlier than for the slow case. The earliest instance of force maximum for NT20 experiments is at 0.85 mm (intermediate velocity), which is 0.06 mm earlier than in the slow case and 0.16 mm earlier than for the fast case. In addition, a slight increase in displacement to fracture is observed in the experiments at high loading velocities. Local axial strain measurements determined from a 1 mm long virtual extensometer (as indicated by solid red dots) are reported on the secondary axis (dashed) in Fig. 5a and c.

Compared to other loading speeds, the slow experiments exhibit a faster rise in the local axial strain as a function of displacement. It is noteworthy that the local strain at fracture is the highest in the slow case, irrespective of the specimen geometry (0.59 for NT20, 0.48 for NT6), while it is lowest for intermediate speeds (0.50 for NT20, 0.40 for NT6). For the fast case, strain levels of 93% of the slow case are observed for NT20 and 95% for NT6.

After evaluating the effective strain,

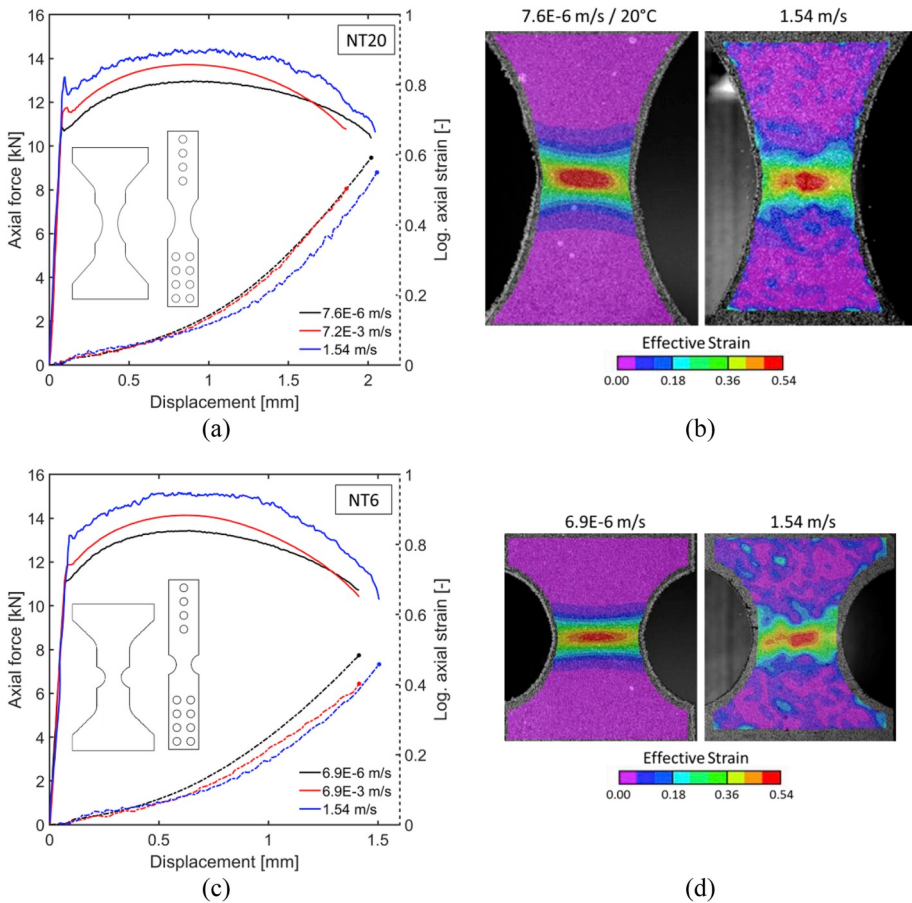


**Fig. 5.** Experimental results from fracture testing of notched specimens at different loading speeds: (a) NT20 and (c) NT6. The force-displacement curves (solid) are plotted along with the local axial strain evolution (dashed) on the secondary ordinate axis. The right column plots show the corresponding effective strain fields right before fracture initiation for (b) NT20 and (d) NT6 specimens.

$$\bar{\varepsilon} = \frac{2}{\sqrt{3}} \sqrt{\varepsilon_I^2 + \varepsilon_I \varepsilon_{II} + \varepsilon_{II}^2} \quad (44)$$

the corresponding surface strain fields just before fracture are shown in the right column of Fig. 5. Note that for both specimen geometries, a zone of localized deformation is observed at the center of the specimen.

### 5.1.2. Experiments at temperatures ranging from 20 to 300 °C

Fig. 6 summarizes the force-displacement curves recorded during slow NT20 experiments for six different temperatures: 20 °C, 60 °C, 120 °C, 180 °C, 240 °C and 300 °C. The most important observation is that the curves are not in hierarchical order with respect to the temperature, i.e. neither the force maximum nor the displacement to fracture exhibit a monotonic dependence on the ambient temperature. However, it is worth noting that the yield point (transition from linear to non-linear specimen response) decreases monotonically as the temperature increases.

When increasing the temperature from room temperature to 60 °C and 120 °C, both the force maximum and the displacement to failure decrease. For 180 °C, the force maximum and the displacement to fracture lie between those for 60 °C and 120 °C (Fig. 6b). The force-displacement curve for 240 °C intersects all curves for lower temperatures. It reaches a force maximum that is 1% higher than that for the 20 °C case, while its displacement to failure is 3% lower than for 20 °C. The experiment at 300 °C reaches the highest force level among all experiments performed. At the same time, a significant increase of 26% in the displacement to fracture as compared to the experiment at room temperature is observed.

Fig. 6c shows a comparison of the effective strain fields at the moment before the onset of fracture. Throughout all six temperatures, the maximum effective strain measured is located at the center of the specimen. Even though the maximum effective strain at 20 °C differs only slightly (< 1%) compared to the 300 °C case, the area with an effective strain higher than 0.45 is wider for the 300 °C case. This indicates a strong change in the hardening behavior at higher temperatures.

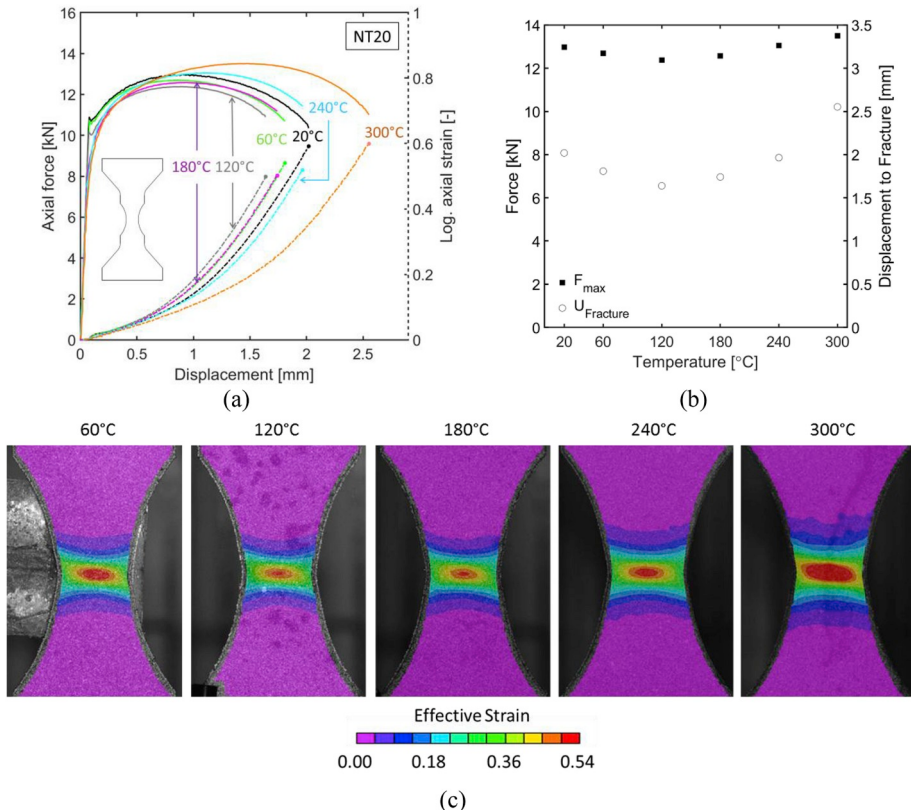


**Fig. 6.** (a) Experimentally determined force-displacement curves (solid) and local axial strain versus displacement curves (dashed) at different temperatures for NT20 specimens. (b) The corresponding maximum force and displacement to fracture are plotted as a function of temperature. The effective surface strain field before the onset of fracture are displayed in (c).

### 5.2. Plasticity model parameters for rate-independent loading at room temperature

Following the procedures outlined in Subsection 3.4, the parameters  $G_{12} = -0.43$ ,  $G_{22} = 0.93$  and  $G_{33} = 3.27$  are chosen to describe the mild anisotropy observed in the Lankford ratios. Table 2 summarizes the Swift-Voce parameters identified from the slow UT and NT20 experiments at room temperature.

### 5.3. Results from machine learning

The three entries of the input vector  $[\bar{\varepsilon}_p, \dot{\bar{\varepsilon}}_p, T]$  are normalized as follows:

- The network input variable  $\bar{x}_1$  is obtained from projecting the logarithm of the equivalent plastic strain onto the interval  $[-7, 1]$ ; this corresponds to an interval of  $\{9 \times 10^{-4} \leq \bar{\varepsilon}_p \leq 2.7\}$ ; note that the logarithm is used to increase the resolution at small strains.
- The network input variable  $\bar{x}_2$  is obtained from projecting the logarithm of the equivalent plastic strain rate onto the interval  $[-9, 10]$ ; this corresponds to an interval of  $\{1.2 \times 10^{-4} s^{-1} \leq \dot{\bar{\varepsilon}}_p \leq 2.2 \times 10^4 s^{-1}\}$ ;
- The network input variable  $\bar{x}_3$  is obtained by projecting the temperature in Kelvin onto the interval  $[293, 593]$ ; this corresponds to an interval of admissible temperatures of  $\{20^\circ C \leq T \leq 320^\circ C\}$ ;

The network output variable  $\bar{y}$  corresponds to the projection of the Johnson-Cook multiplier  $k_{NN}$  onto the interval  $[0.5, 1.5]$ , the assumed minimum and maximum attainable value of the multiplier.

The pre-training pseudo dataset is an estimation based on the NT20 experimental data (Tables 3–5). This initial guess is created by dividing the maximum force for each experiment by the maximum force of the slow NT20 experiment at room temperature. It follows that the target for the latter experiment is an array of 1, as shown in Table 3.

Preliminary training runs have been performed using different network architectures. The results for three layer networks (Fig. 7a) show that with more than 10 neurons per layer, the achieved mean squared error reaches a plateau, indicating no merit brought by increasing the network size. When each layer has the same number of neurons (Fig. 7b), a three-layer network performs consistently better than a single and two-layer network. We therefore chose a network with  $M = 3$  hidden layers, with each layer containing  $P = 10$  neurons to capture the material response. Adding bias neurons to the input and hidden layers (as discussed in

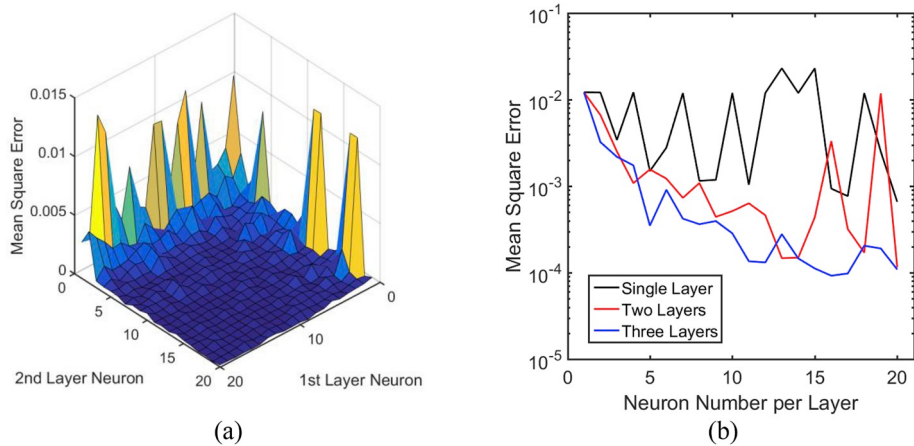


**Fig. 7.** Effect of network topology: (a) Performance of a three-layer network trained up to 200 epochs (fixing  $P = 5$  neuron for the third layer). (b) Comparison of a single-layer, two-layer and three-layer network with same number of neurons per layer.

**Table 6**  
Summary of network training parameters.

$\eta_L$ [-]	$\eta^+$ [-]	$\eta^-$ [-]	$\Delta_{\min}$ [-]	$\Delta_{\max}$ [-]	$\mu_M$ [-]
0.1	1.2	0.8	0.001	1000	0.05

session 3.2.2), the network layout becomes [4,11,11,11,1]. This choice corresponds to a total of  $4 \times 11 + 11 \times 11 + 11 \times 11 + 11 \times 1 = 297$  model parameters. The network training parameters are summarized in Table 6. After terminating the pre-training involving 30 epochs (completed in less than 5min on a personal computer), the pre-trained neural network is implemented into a user material subroutine (VUMAT) along with a return mapping scheme for solving the three-dimensional constitutive equations with non-associated flow rule. In the return mapping scheme, the partial derivative of the neural network function  $k_{NN}$  with respect to the components of the input layer  $\mathbf{H}^{(0)}$  (strain, strain rate and temperature) must be known. After applying the chain rule (back propagation), we obtain

$$\frac{\partial k^{NN}}{\partial \mathbf{H}^{(0)}} = \left( \frac{\partial \mathbf{H}^{(3)}}{\partial \mathbf{H}^{(2)}} \frac{\partial \mathbf{H}^{(2)}}{\partial \mathbf{H}^{(1)}} \frac{\partial \mathbf{H}^{(1)}}{\partial \mathbf{H}^{(0)}} \right)^T \frac{\partial k^{NN}}{\partial \mathbf{H}^{(3)}}, \quad (45)$$

while the matrices  $\partial \mathbf{H}^{(k)} / \partial \mathbf{H}^{(k-1)}$  read

$$\left\{ \frac{\partial \mathbf{H}^{(k)}}{\partial \mathbf{H}^{(k-1)}} \right\}_{ij} = \frac{\partial H_i^{(k)}}{\partial H_j^{(k-1)}} = [1 - (H_i^{(k)})^2] W_{ij}^{(k-1)}. \quad (46)$$

It is worth noting that the related computational costs for evaluating these network derivatives are higher than for a conventional Johnson-Cook function, but still reasonable due to the simplicity of the mathematical expressions. The results obtained from finite element simulations of the NT20 experiments using the pre-trained model are shown in Fig. 8. While the overall trends, i.e. the increase in stress with strain rate, and the non-monotonic temperature dependence are captured by this initial guess, the actual material behavior, especially at large strains, is still poorly approximated as far as the difference between the measured and the predicted forces are concerned.

The final training process of the neural network involves the simulation of eight NT20 experiments, i.e. room temperature experiments at three different strain rates and quasi-static experiments at six different temperatures (Figs. 5a and 6a). Taking advantage of the symmetry of the mechanical system, only one eighth of the tensile specimen is meshed with solid elements (Fig. 3). Eight first-order reduced-integration elements (type C3D8R from Abaqus library) are used over half the specimen thickness and 50 elements are used along the sample mid-plane, each with an element length of 0.1 mm. This results in overall 400 elements being used to relate the error between the experimentally and numerically obtained force to a stress error usable for training the neural network (Eq. (43)). A total of 200 data points are extracted from each measured force-displacement curve, i.e. the model training data comprised 1600 data points. Using 12 CPUs for each experiment ( $8 \times 12 = 96$  CPUs), the convergence criterion (mean squared force error  $< 0.01$  kN<sup>2</sup>) for training is met after 101 epochs. In other words, 101 rounds of FE simulations are performed to identify the neural network parameters. On a high performance cluster, this task is completed in 97 h (corresponding to 9312 CPU core hours). For comparison, we note that Roth and Mohr (2014) performed 264 epochs to identify the parameters of a Johnson-Cook model based on FE simulations of three experiments using gradient-free simplex algorithm.

Fig. 9 shows that the simulation curves (solid lines) for all NT20 experiments now lie on top of the corresponding experimental

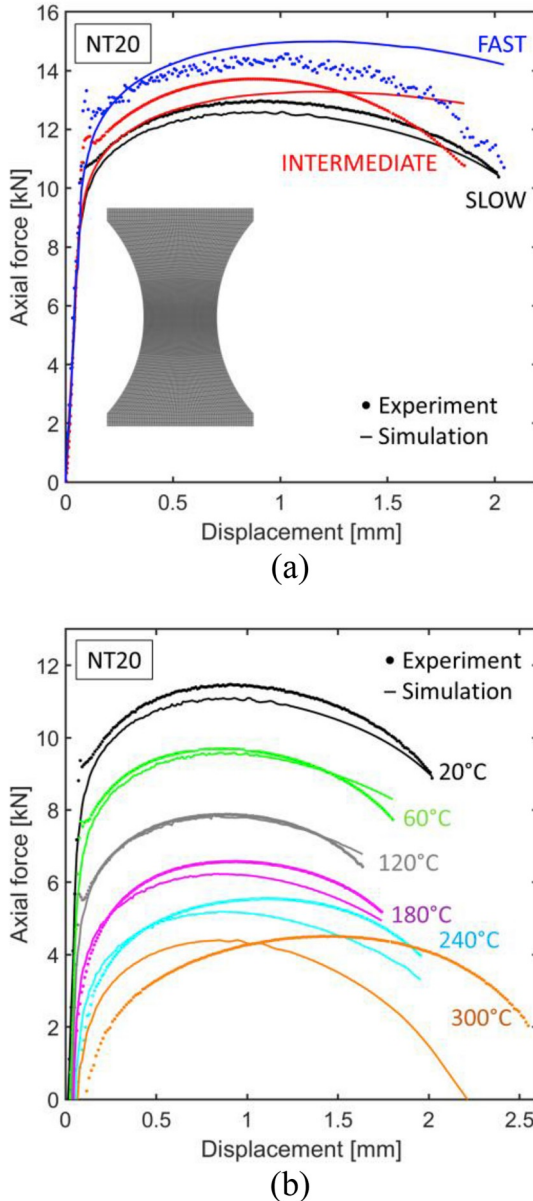


**Fig. 8.** Results after completing pre-training: experimental and numerically-predicted force-displacement curves for NT20 specimens. Experiments for different strain rates are shown in (a). Experiments at elevated temperatures are shown in (b). The temperature experiments are shifted by 1.5 kN for better readability.

curves (solid dots). The maximum error on the force-displacement curve occurs at the intermediate loading case (Fig. 9a), with the maximum error being 1.5%. Even though they have not been used for the training of the model, a good agreement is also obtained on the local surface strain measurements, thereby partially validating the applicability of the plasticity model (Fig. 9b and d). An overestimation of the local surface strain right before the onset of fracture can be observed for intermediate (7%) and fast (10%) loading. A difference of 11% and 8% is also witnessed in the case of 300 °C and 120 °C, respectively (Fig. 9d). For all other loading cases, the local strains predicted by the finite element simulation are within 4% of the respective experimental measurements.

To further validate the machine-learning based constitutive model, it is used to simulate experiments on NT6 specimens for slow, intermediate and fast loading. Even though none of the NT6 specimens had been used for training (independent testing data), we observe a good agreement of the numerically-predicted and experimentally-measured force-displacement curves (Fig. 10a). In the slow case, the predicted force is overestimated by 4% after the force maximum, while a net difference of 0.07 is observed when comparing the local strains in the post-necking range for the intermediate and fast experiments (Fig. 10b).

To reveal the material behavior identified by the machine-learning based model, we visualize the deformation resistance as a function of the equivalent plastic strain, the strain rate and the temperature. Note that the function  $k = k(\dot{\varepsilon}_p, \dot{\varepsilon}_p, T)$  corresponds to a

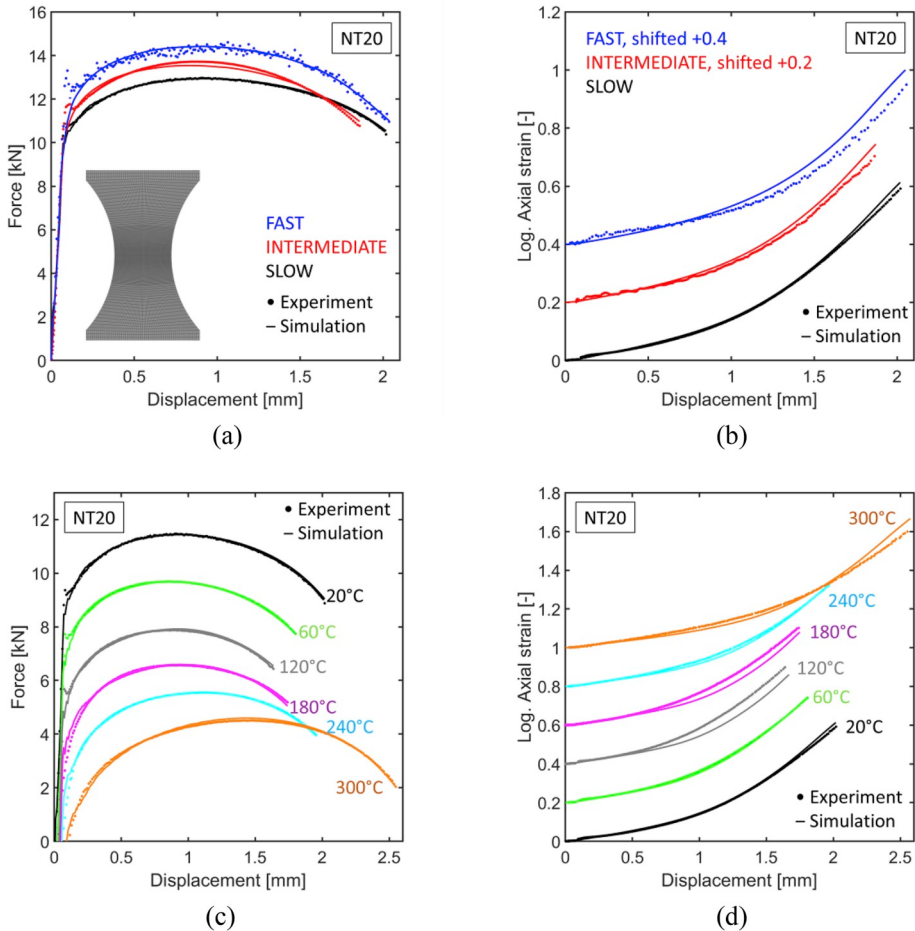


**Fig. 9.** Result after completing final training: experimental and numerically-predicted results for NT20 specimens. Experiments at different strain rates are simulated to generate (a) force-displacement curves, and (b) local strain histories. Experiments at elevated temperatures are shown in (c) force-displacement curves and (d) local strain histories. The temperature force-displacement curves are shifted by 1.5 kN for better readability. The axial strain histories are also shifted by 0.2.

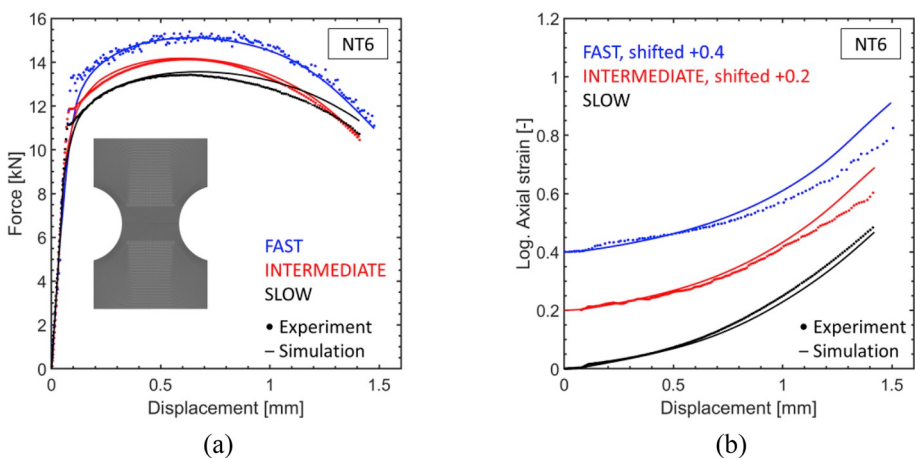


**Fig. 10.** Testing dataset: NT6 specimen at different loading speeds (a) force-displacement; (b) surface strain histories. The local axial strain histories in (b) are shifted by 0.2 for better readability.

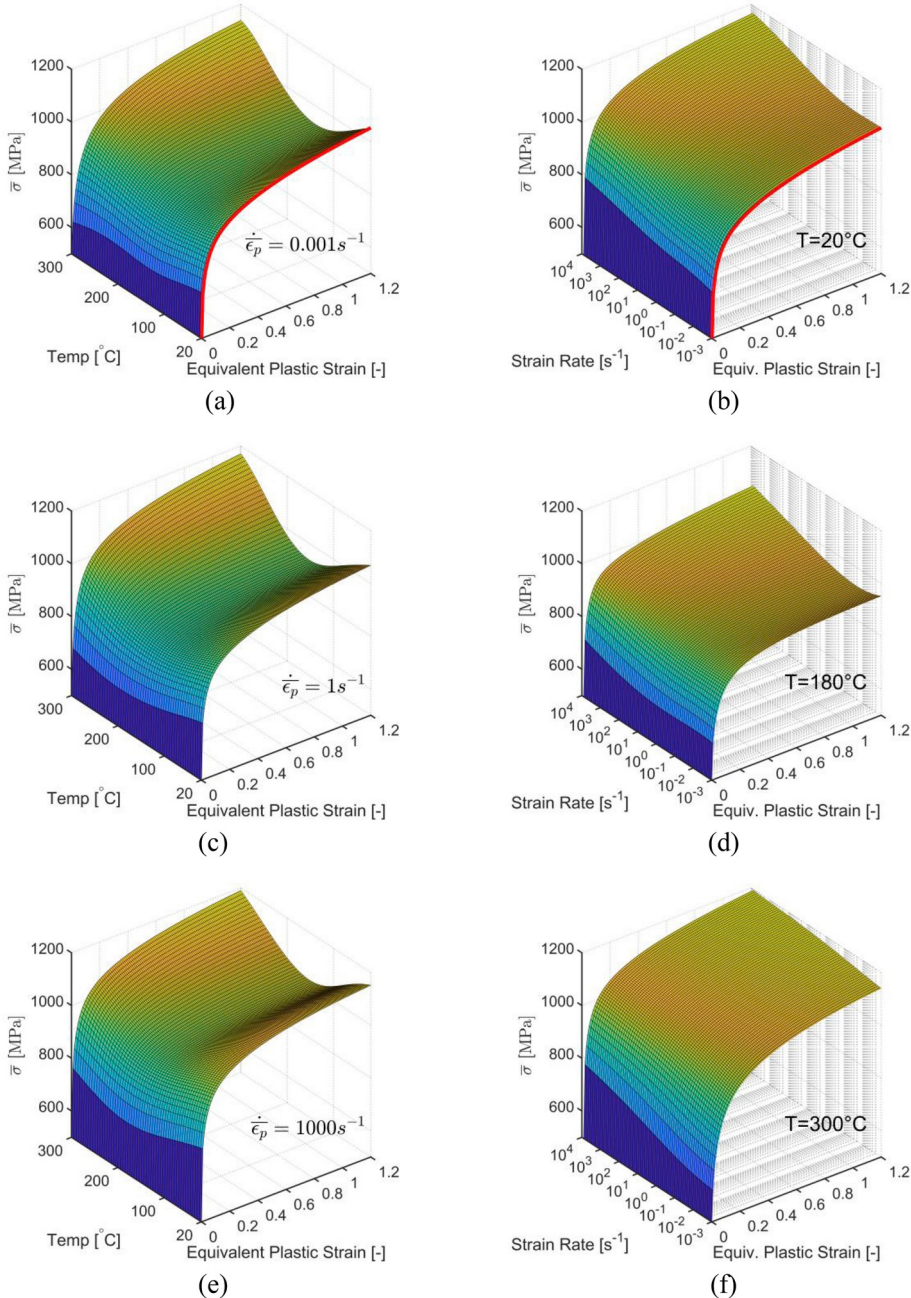
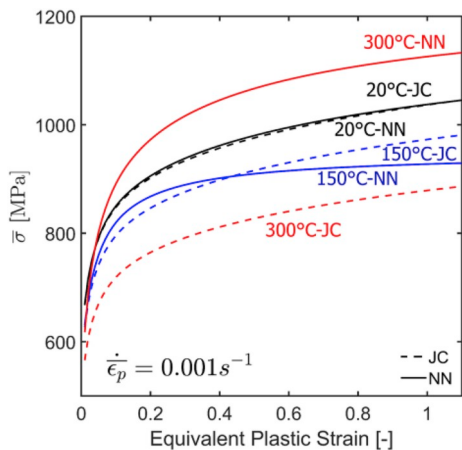
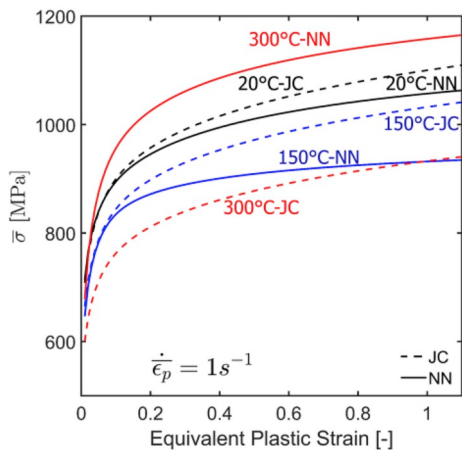


**Fig. 11.** Deformation resistance as a function of strain rate and temperature as identified through machine learning. The solid red line in (a) and (b) represents the model response at room temperature for quasi-static loading conditions. (For interpretation of the references to colour in this figure legend, the reader is referred to the Web version of this article.)

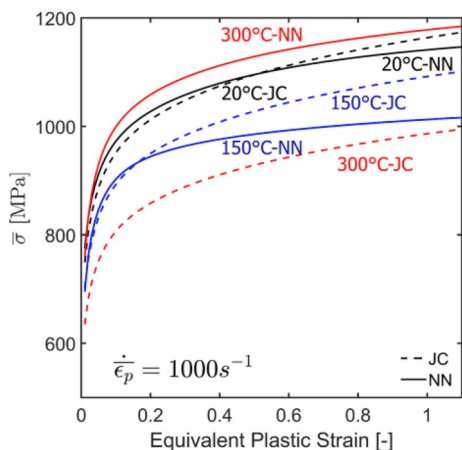
surface in  $\mathbb{R}^4$ , while an object in  $\mathbb{R}^3$  is obtained when fixing one of the arguments. The plot for a fixed strain rate of  $\dot{\epsilon}_p = 10^{-3}/s$ ,  $\dot{\epsilon}_p = 1/s$  and  $\dot{\epsilon}_p = 10^3/s$  (Fig. 11a,c,d) shows the non-monotonic effect of the temperature on the deformation resistance over a wide range of strain rates. It also demonstrates that the trained neural network maintains the monotonicity in strain, i.e. for a fixed strain rate and temperature, the deformation resistance increases as a function of the equivalent plastic strain. As expected from the experimental data, the model suggests a decrease in the deformation resistance as the temperature increases before reaching a minimum at a temperature of about  $155^{\circ}C$ , beyond which a positive temperature effect is observed. Across all three strain rates, a plateau shaped hardening behavior at  $150^{\circ}C$  is observed, which is very similar to the Voce-type of hardening law introduced earlier. The strain rate effects at room temperature ( $T = 20^{\circ}C$ ),  $T = 180^{\circ}C$  and  $T = 300^{\circ}C$  are depicted in Fig. 11 b, d and f. It is similar to the original Johnson-Cook model as far as its monotonicity is concerned, but it is neither of logarithmic nature nor independent of the



(a)



(b)



(c)

**Fig. 12.** Comparison of standard Johnson-Cook (JC) and neural-network (NN) based model for different strain rates: (a) 0.001/s, (b) 1/s and (c) 1000/s. Note that the NN based plasticity model exhibits a non-monotonic temperature response at both quasi-static and dynamic strain rates.

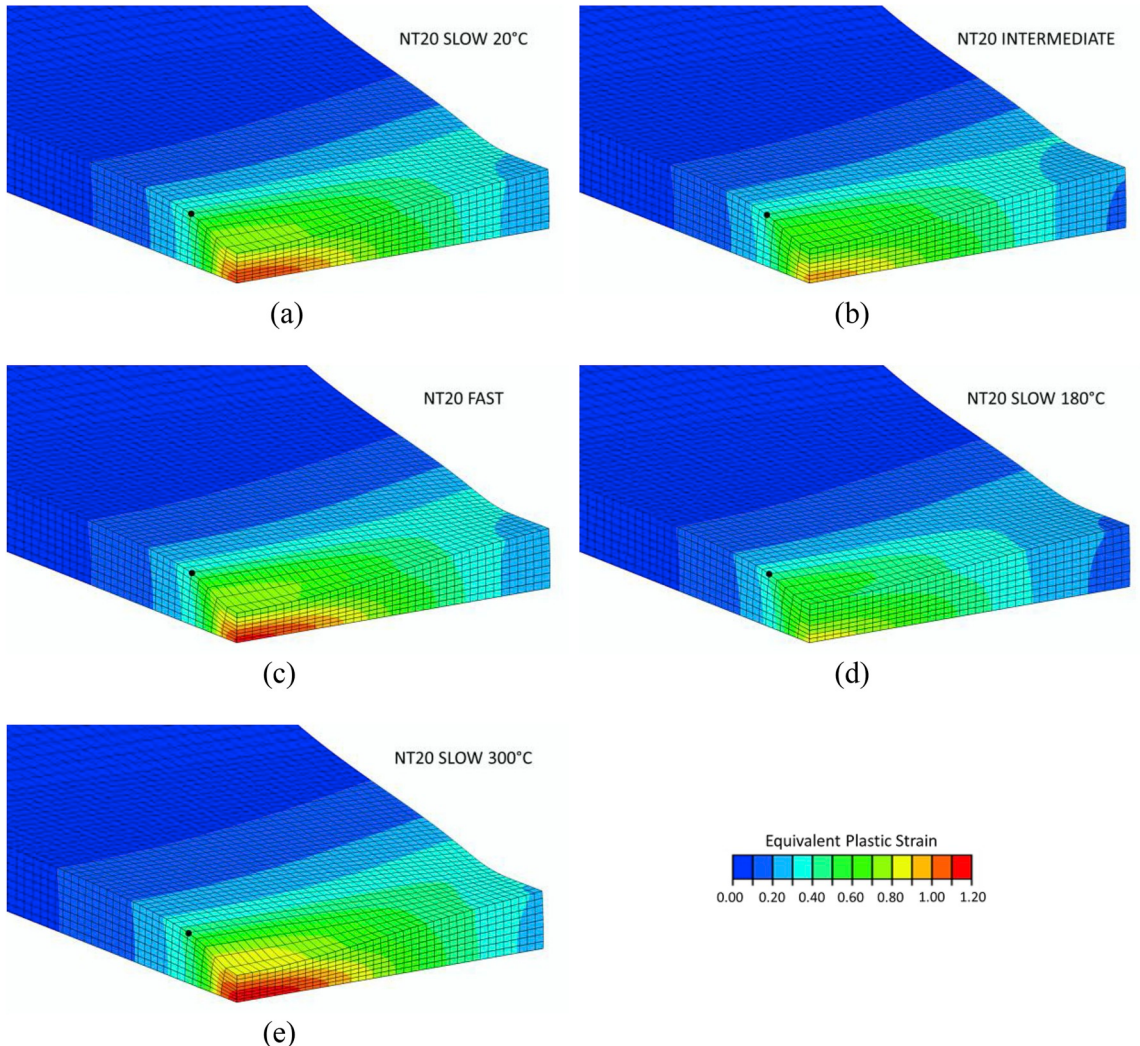


**Fig. 13.** Contour plots of the equivalent plastic strain at the onset of fracture for selected loading cases of the NT20 specimens. The location of the surface strain extensometers is indicated by black dots.

plastic strain. Overall, it is noteworthy that, despite the large range and wide spacing (regarding the temperatures and strain rates) of the training data, the machine-learning algorithm came up with a particularly smooth function. Specifically, with three orders of magnitude difference on the strain rates, the neural network does not create extra peaks or valleys in the regions not covered by the training data.

For comparison purposes, we also calibrated the modified Johnson-Cook model of Roth and Mohr (2014) based on the current experimental data. In Eq. (13), it makes use of the same Swift-Voce strain hardening term  $k_{SV}[\dot{\varepsilon}_p]$ , while the neural network term is substituted through a standard Johnson-Cook parametric form

$$k_{NN}[\dot{\varepsilon}_p, \dot{\dot{\varepsilon}}_p, T] \rightarrow \left(1 + C \ln\left(\frac{\dot{\varepsilon}_p}{\dot{\varepsilon}_0}\right)\right) \left(1 - \left(\frac{T - T_r}{T_m - T_r}\right)\right)^m. \quad (47)$$

Fig. 12 shows selected stress-strain curves as predicted by the calibrated neural network (solid lines) and the standard Johnson-Cook model (dashed lines). While reasonable agreement of both models is observed at room temperature (at all three strain rates, compare black curves in Fig. 12a–c), there is a significant mismatch at elevated temperatures. For an initial temperature of 150 °C, the stress estimates are still close at small strains, but at large strains the JC-model overestimates the strain hardening significantly. Even more pronounced differences exceeding 50% in stress are observed at 300 °C. Due to the monotonicity of the JC temperature term, the 300 °C curves for the JC model lies below that for 150 °C. Conversely, the neural network model predicts the highest stress levels for 300 °C which is in line with the trend observed experimentally.

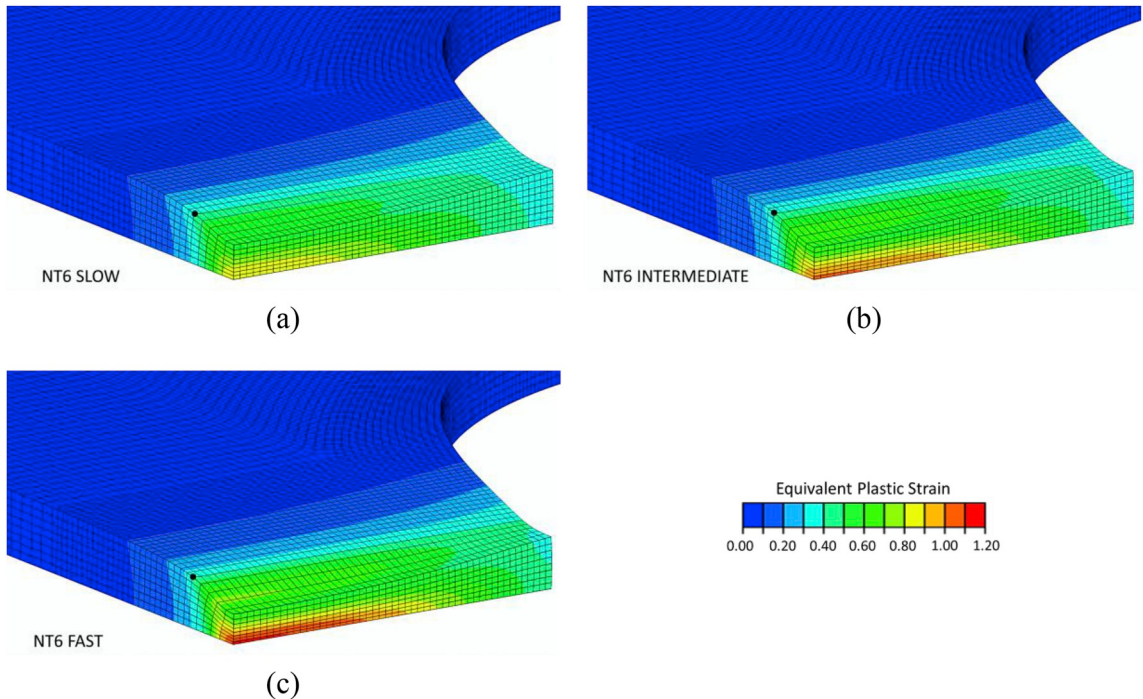


**Fig. 14.** Contour plots of the equivalent plastic strain at the onset of fracture for all NT6 specimens. The location of the surface strain extensometers is depicted by black dots. The numerical simulations of the NT6 experiments are used to validate the neural network based plasticity model.

#### 5.4. Effect of temperature on strain to fracture

The results from the finite element simulations of the NT20 experiments at different temperatures are further exploited to determine the effect of the temperature on the ductility of the DP800 steel. Fig. 13 shows selected deformed FE meshes with contour plots of equivalent plastic strain before fracture for NT20 samples. The black dots indicate the current location of the surface extensometer. The deformation localizes within a small zone at the center of the specimen. For the intermediate (Fig. 13b) and slow loading cases at 180 °C (Fig. 13d), the equivalent plastic strain at the onset of fracture is significantly lower than in the other loading conditions. The corresponding contour plots of the equivalent plastic strain for the NT6 geometry are displayed in Fig. 14.

The evolution of the equivalent plastic strain  $\bar{\varepsilon}_p$ , strain rate  $\dot{\varepsilon}_p$ , temperature  $T$ , stress triaxiality  $\eta$  and Lode angle parameter  $\theta$  are extracted from each simulation at the location where the highest equivalent plastic strain is attained (i.e. on the mid-plane at the specimen center). Fig. 15 summarizes the extracted loading paths. They all lie approximately on top of each other as far as the evolution of the equivalent plastic strain as a function of the stress state and strain rate are concerned (Fig. 15a and c). The variation of the fracture strain as a function of the temperature is best visible in Fig. 15d. Note that the end of each loading path corresponds to the instant of fracture initiation (implying that fracture is assumed to initiate in the experiments when the force drops abruptly). The results reveal that the ductility is a non-monotonic function of the temperature. It decreases from  $\bar{\varepsilon}_f = 1.14$  to 0.81 when increasing the temperature from 20 to 120 °C. For higher temperatures, the ductility then increases again reaching a value of  $\bar{\varepsilon}_f = 1.20$  at 300 °C.

#### 5.5. Remark regarding the effect of strain rate on strain to fracture

Further analysis is needed to quantify the effect of the strain rate on the strain to fracture. The comparison of the loading paths to fracture extracted from the slow, intermediate and fast NT20 experiments (Fig. 15c) shows approximately the same ductility for the slow ( $\bar{\varepsilon}_f = 1.14$ ) and fast ( $\bar{\varepsilon}_f = 1.20$ ) experiments, while a lower strain to fracture of  $\bar{\varepsilon}_f = 0.96$  is observed in the intermediate velocity experiment. The estimated temperatures at the instants of fracture initiation are 183 °C and 233 °C in the intermediate speed and fast experiments. It could thus be argued that the temperature effect led to the reduced ductility in the intermediate experiment, while the effect of strain rate on the strain to fracture could still be of monotonic nature. However, none such conclusion may be drawn based on the current experimental evidence since the effect of temperature on the ductility might be strain rate dependent. Further experimental work and analysis (e.g. high strain rate experiments at different temperatures) are needed to gain the necessary insight.

#### 5.6. Remark regarding the computational efficiency and value-added by neural network approach

The major advantage of the neural network over parametric models is that it requires no prior assumption on the mathematical formulation between the input and output variables. Without model bias, the neural network is able to capture the stress-strain

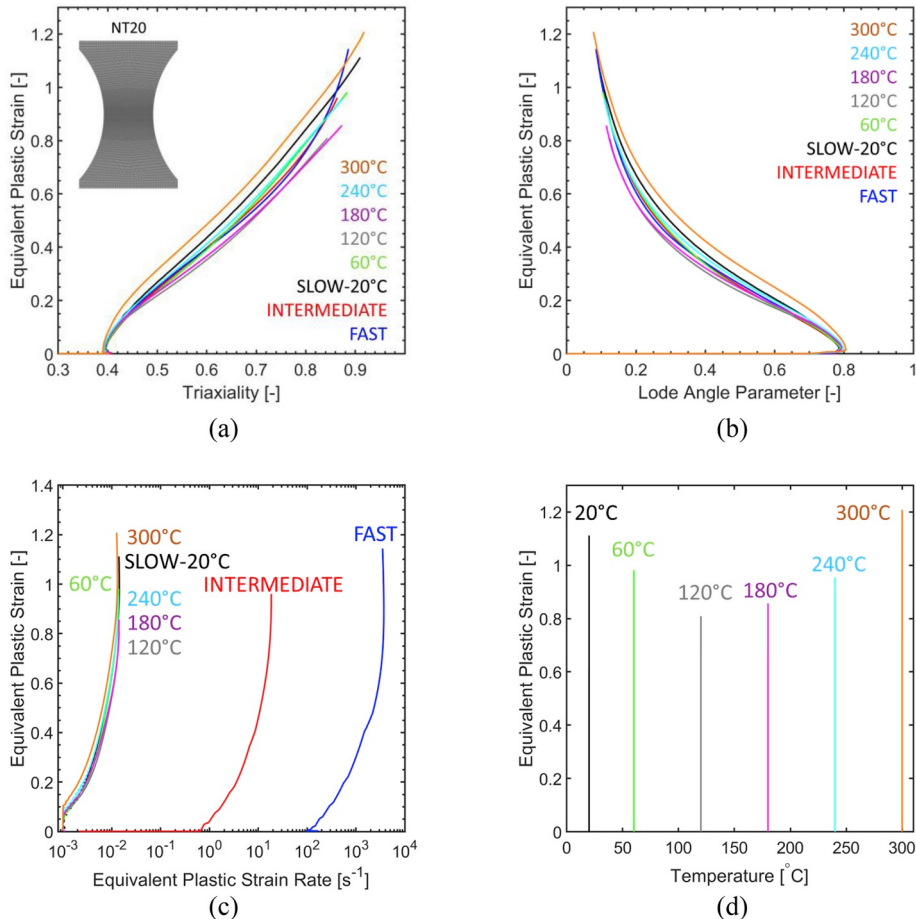


**Fig. 15.** Loading paths to fracture extracted from NT20 simulations: The evolution of equivalent plastic strain as a function of (a) stress triaxiality, (b) Lode angle parameter and (c) strain rate. The non-monotonic dependency of equivalent plastic strain to fracture as a function of temperature is showcased in (d). The end of the solid lines corresponds to the instant of fracture initiation.

response under different rates and temperatures. In the present work, the machine learning approach is successfully executed using a FE-based cost function, thereby enabling the material model identification based on experiments with non-uniform mechanical fields and variable temperature and strain rate histories.

For a simulation of an NT20 experiment with 12 cores on a high performance cluster, the neural network based subroutine takes about 30min, while a subroutine with JC-type of parametric hardening function takes about 21min. While there might still be some potential in developing more efficient algorithms for the return mapping with a neural network based hardening function, it is worth noting that the neural network may also serve as a basis for calibrating computationally-efficient parametric models or lookup table models (e.g. the Abaqus material model available under the keyword \*rate dependent, type = yield ratio). The prime value added by the machine learning at this stage is not its computational efficiency, but its ability to unveil the intrinsic response of a material in the case of convoluted experimental data.

## 6. Summary and conclusions

Tension experiments of notched specimens at temperatures ranging from 20 to 300 °C revealed a non-monotonic dependence of the strain hardening response for DP800 steel. Neither standard physics-based (e.g. Zerilli-Armstrong) nor phenomenological models (e.g. Johnson-Cook) can describe this unconventional behavior. We therefore used a machine-learning approach to identify a modified Johnson-Cook model for describing the strain rate and temperature dependent plasticity of DP steels. A neural network with three hidden layers of 10 neurons each is identified in a two-step procedure. A first set of network parameters is obtained by applying a standard back-propagation training algorithm for fitting approximate stress-strain curves for different temperatures and strain rates. Then, in a second training step, the neural network is implemented into a user material subroutine together with the return mapping algorithm for solving the three-dimensional constitutive equations. Model parameters providing highly accurate predictions of all experimentally-measured force-displacement curves are then obtained by repeatedly launching full-3D finite element simulations during the training of the neural network.

As final result of the machine-learning, a hardening law is obtained that expresses the yield stress as a function of the equivalent plastic strain, strain rate and temperature. It exhibits a non-monotonic dependence on the temperature, with a minimum in deformation resistance at temperatures around 155 °C. The hardening law shows a monotonic dependence on the strain rate, but with a rate sensitivity that varies as function of the strain and temperature. In addition to analyzing the plastic material response, the loading paths to fracture are extracted from the finite element simulations with the machine learning based constitutive model. The simulations of the slow experiments revealed that the strain to fracture decreases by about 28% when increasing the temperature from 20 to 120 °C, before it increases again reaching about the same level as at room temperature when the temperature attains 300 °C.

Aside from revealing the important non-monotonic effect of the temperature on the ductility of dual phase steel, the present work demonstrates that machine learning allows for the identification of a hardening law through hybrid experimental-numerical analysis without introducing any model bias prior to calibration. This bias-free identification is an important advantage of the neural network approach over conventional parametric hardening laws. Once the neural network model is identified from experiments with heterogeneous mechanical fields, stress-strain curves for idealized conditions (e.g. constant strain rate and temperature) can be generated and used to come up with a suitable parametric or look-up table model. Even though the neural network model can be directly used in large scale FE computations, parametric hardening laws are expected to yield a higher computational efficiency.

## Acknowledgments

The authors would like to thank Ms Franziska Siebenbrock for her help with performing the experiments. Thanks are also due to Dr. Thomas Tancogne-Dejean and Dr. Colin Bonatti for valuable discussions. The partial financial support through the Swiss National Science Foundation SNF Grant 200021-165939 is gratefully acknowledged.

## Appendix A. Supplementary data

Supplementary data to this article can be found online at <https://doi.org/10.1016/j.ijplas.2019.02.012>.

## References

- Abed, F., Makarem, F., 2012. Comparisons of constitutive models for steel over a wide range of temperatures and strain rates. *J. Eng. Mater. Technol.* 134, 21001. <https://doi.org/10.1115/1.4006171>.
- Abedini, A., Butcher, C., Worswick, M.J., 2018. Experimental fracture characterisation of an anisotropic magnesium alloy sheet in proportional and non-proportional loading conditions. *Int. J. Solids Struct.* 144 (145), 1–19. Available at: <https://doi.org/10.1016/j.ijsolstr.2018.04.010>.
- Al-Haik, M.S., Hussaini, M.Y., Garmestani, H., 2006. Prediction of nonlinear viscoelastic behavior of polymeric composites using an artificial neural network. *Int. J. Plast.* 22 (7), 1367–1392.
- Bai, Y., Wierzbicki, T., 2008. A new model of metal plasticity and fracture with pressure and Lode dependence. *Int. J. Plast.* 24, 1071–1096. <https://doi.org/10.1016/j.ijplas.2007.09.004>.
- Baral, M., Hama, T., Knudsen, E., Korkolis, Y.P., 2018. Plastic deformation of commercially-pure titanium: experiments and modeling. *Int. J. Plast.* 105, 164–194. <https://doi.org/10.1016/j.ijplas.2018.02.009>.
- Ben-David, S., Shalev-Shwartz, S., 2014. Understanding Machine Learning: from Theory to Algorithms. <https://doi.org/10.1017/CBO9781107298019>.
- Borvik, T., Hopperstad, O.S., Berstad, T., Langseth, M., 2001. A computational model of viscoplasticity and ductile damage for impact and penetration. *Eur. J. Mech. A Solid.* 20, 685–712. [https://doi.org/10.1016/S0997-7538\(01\)01157-3](https://doi.org/10.1016/S0997-7538(01)01157-3).
- Brüning, M., Chyra, O., Albrecht, D., Driemeier, L., Alves, M., 2008. A ductile damage criterion at various stress triaxialities. *Int. J. Plast.* 24, 1731–1755. <https://doi.org/10.1016/j.ijplas.2007.12.001>.
- Brüning, M., Gerke, S., Schmid, M., 2018. Damage and failure at negative stress triaxialities: experiments, modeling and numerical simulations. *Int. J. Plast.* 102, 70–82. <https://doi.org/10.1016/j.ijplas.2017.12.003>.
- Cao, Y., Ahlström, J., Karlsson, B., 2015a. The influence of temperatures and strain rates on the mechanical behavior of dual phase steel in different conditions. *J. Mater. Res. Technol.* 4, 68–74. <https://doi.org/10.1016/j.jmrt.2014.11.001>.
- Cao, Y., Karlsson, B., Ahlström, J., 2015b. Temperature and strain rate effects on the mechanical behavior of dual phase steel. *Mater. Sci. Eng., A* 636, 124–132. <https://doi.org/10.1016/j.msea.2015.03.019>.
- Chatterjee, A., et al., 2018. Role of hierarchical martensitic microstructure on localized deformation and fracture of 9Cr-1Mo steel under impact loading at different temperatures. *Int. J. Plast.* 104, 104–133. (October 2017) Available at: <https://doi.org/10.1016/j.ijplas.2018.02.002>.
- Conrad, H., 1964. Thermally activated deformation of metals. *JOM* 16, 582–588. <https://doi.org/10.1007/BF03378292>.
- Dunand, M., Mohr, D., 2017. Predicting the rate-dependent loading paths to fracture in advanced high strength steels using an extended mechanical threshold model. *Int. J. Impact Eng.* 108, 272–285. <https://doi.org/10.1016/j.ijimpeng.2017.02.020>.
- Durrenberger, L., Klepaczko, J.R., Rusinek, A., 2007. Constitutive modeling of metals based on the evolution of the strain-hardening rate. *J. Eng. Mater. Technol.* 129, 550. <https://doi.org/10.1115/1.2772327>.
- Erice, B., Pérez-Martín, M.J., Gálvez, F., 2014. An experimental and numerical study of ductile failure under quasi-static and impact loadings of Inconel 718 nickel-base superalloy. *Int. J. Impact Eng.* 69, 11–24. <https://doi.org/10.1016/j.ijimpeng.2014.02.007>.
- Follansbee, P.S., Kocks, U.F., 1988. A constitutive description of the deformation of copper based on the use of the mechanical threshold stress as an internal state variable. *Acta* 36, 81–93. [https://doi.org/10.1016/0001-6160\(88\)90030-2](https://doi.org/10.1016/0001-6160(88)90030-2).
- Forni, D., Chiaia, B., Cadoni, E., 2016. High strain rate response of S355 at high temperatures. *Mater. Des.* 94, 467–478. <https://doi.org/10.1016/j.matdes.2015.12.160>.
- Fourmeau, M., Borvik, T., Benallal, A., Hopperstad, O.S., 2013. Anisotropic failure modes of high-strength aluminium alloy under various stress states. *Int. J. Plast.* 48, 34–53. <https://doi.org/10.1016/j.ijplas.2013.02.004>.
- Gruben, G., Langseth, M., Fagerholt, E., Hopperstad, O.S., 2016. Low-velocity impact on high-strength steel sheets: an experimental and numerical study. *Int. J. Impact Eng.* 88, 153–171. <https://doi.org/10.1016/j.ijimpeng.2015.10.001>.
- Gündüz, S., Tosun, A., 2008. Influence of straining and ageing on the room temperature mechanical properties of dual phase steel. *Mater. Des.* 29, 1914–1918. <https://doi.org/10.1016/j.matdes.2008.04.028>.
- Huang, G. Bin, 2003. Learning capability and storage capacity of two-hidden-layer feedforward networks. *IEEE Trans. Neural Netw.* 14, 274–281. <https://doi.org/10.1109/TNN.2003.809401>.
- Huh, H., Ahn, K., Lim, J.H., Kim, H.W., Park, L.J., 2014. Evaluation of dynamic hardening models for BCC, FCC, and HCP metals at a wide range of strain rates. *J.*

- Mater. Process. Technol. 214, 1326–1340. <https://doi.org/10.1016/j.jmatprotec.2014.02.004>.
- Hüper, T., Endo, S., Ishikawa, N., Osawa, K., 1999. Effect of volume fraction of constituent phases on the stress-strain relationship of dual phase steels. *ISIJ Int.* 39 (3), 288–294.
- Jenab, A., Sari Sarraf, I., Green, D.E., Rahmaan, T., Worswick, M.J., 2016. The Use of genetic algorithm and neural network to predict rate-dependent tensile flow behaviour of AA5182-sheets. *Mater. Des.* 94, 262–273. <https://doi.org/10.1016/j.matdes.2016.01.038>.
- Johnson, G.R., Cook, W.H., 1983. A constitutive model and data for metals subjected to large strains, high strain rates and high temperatures. In: 7th International Symposium on Ballistics, the Hague, pp. 541–547.
- Kajberg, J., Sundin, K.G., 2013. Material characterisation using high-temperature Split Hopkinson pressure bar. *J. Mater. Process. Technol.* 213, 522–531. <https://doi.org/10.1016/j.jmatprotec.2012.11.008>.
- Kessler, B.S., El-Gizawy, A.S., Smith, D.E., 2007. Erratum: “incorporating neural network material models within finite element analysis for rheological behavior prediction”. *J. Pressure Vessel Technol.* 129 (1), 58–65. *J. Press. Vessel Technol.* 129, 342. <https://doi.org/10.1115/1.2728894>.
- Khan, A.S., Liang, R., 1999. Behaviors of three BCC metal over a wide range of strain rates and temperatures: experiments and modeling. *Int. J. Plast.* 15, 1089–1109. [https://doi.org/10.1016/S0749-6419\(99\)00030-3](https://doi.org/10.1016/S0749-6419(99)00030-3).
- Kocks, U.F., Argon, A.S., Ashby, M.F., 1975. *Thermodynamics and Kinetics of Slip*. Pergamon Press, Oxford (London; Edinburg; New York; Toronto).
- Koh, S., Kim, H., Tummala, R., Hajali, R., Saxena, A., 2007. Nonlinear constitutive models from nanoindentation tests using artificial neural networks. *Int. J. Plast.* 24, 371–396. <https://doi.org/10.1016/j.ijplas.2007.02.001>.
- Kohar, C.P., Brahme, A., Imbert, J., Mishra, R.K., Inal, K., 2017. Effects of coupling anisotropic yield functions with the optimization process of extruded aluminium front rail geometries in crashworthiness. *Int. J. Solids Struct.* 128, 174–198. Available at: <https://doi.org/10.1016/j.ijsolstr.2017.08.026>.
- Kohar, C.P., Zhumagulov, A., Brahme, A., Worswick, M.J., Mishra, R.K., Inal, K., 2016. Development of high crush efficient, extrudable aluminium front rails for vehicle lightweighting. *Int. J. Impact Eng.* 95, 17–34. Available at: <https://doi.org/10.1016/j.ijimpeng.2016.04.004>.
- Korkolis, Y.P., Kyriakides, S., 2009. Path-dependent failure of inflated aluminum tubes. *Int. J. Plast.* 25, 2059–2080. <https://doi.org/10.1016/j.ijplas.2008.12.016>.
- Kuang, C. fu, Zheng, Z. wang, Zhang, G. ting, Chang, J., Zhang, S. gen, Liu, B., 2016. Effects of overaging temperature on the microstructure and properties of 600 MPa cold-rolled dual-phase steel. *Int. J. Miner. Metall. Mater.* 23, 943–948. <https://doi.org/10.1007/s12613-016-1310-4>.
- Lee, J.Y., Steglich, D., Lee, M.G., 2018. Fracture prediction based on a two-surface plasticity law for the anisotropic magnesium alloys AZ31 and ZE10. *Int. J. Plast.* 105, 1–23. (October 2017) Available at: <https://doi.org/10.1016/j.ijplas.2017.10.002>.
- Li, S., et al., 2018. Anisotropic fracture of advanced high strength steel sheets: experiment and theory. *Int. J. Plast.* 103, 95–118 (December 2017).
- Liu, Z.G., Wong, W.H., Guo, T.F., 2016. Void behaviors from low to high triaxialities: transition from void collapse to void coalescence. *Int. J. Plast.* 84, 183–202. Available at: <https://doi.org/10.1016/j.ijplas.2016.05.008>.
- Lou, Y., Yoon, J.W., 2017. Anisotropic ductile fracture criterion based on linear transformation. *Int. J. Plast.* 93, 3–25. Available at: <https://doi.org/10.1016/j.ijplas.2017.04.008>.
- Lou, Y., Yoon, J.W., 2018. Anisotropic yield function based on stress invariants for BCC and FCC metals and its extension to ductile fracture criterion. *Int. J. Plast.* 101, 125–155. (October 2017) Available at: <https://doi.org/10.1016/j.ijplas.2017.10.012>.
- Lou, Y., Yoon, J.W., Huh, H., 2014. Modeling of shear ductile fracture considering a changeable cut-off value for stress triaxiality. *Int. J. Plast.* 54, 56–80. <https://doi.org/10.1016/j.ijplas.2013.08.006>.
- Malcher, L., Andrade Pires, F.M., César De Sá, J.M.A., 2014. An extended GTN model for ductile fracture under high and low stress triaxiality. *Int. J. Plast.* 54, 193–228. <https://doi.org/10.1016/j.ijplas.2013.08.015>.
- Marcadet, S.J., Mohr, D., 2015. Effect of compression–tension loading reversal on the strain to fracture of dual phase steel sheets. *Int. J. Plast.* 72, 21–43. Available at: <http://www.sciencedirect.com/science/article/pii/S0749641915000716>.
- Morin, D., Hopperstad, O.S., Benallal, A., 2018. On the description of ductile fracture in metals by the strain localization theory. *Int. J. Fract.* 209 (1–2), 27–51.
- Piao, M., Huh, H., Lee, I., Ahn, K., Kim, H., Park, L., 2016. Characterization of flow stress at ultra-high strain rates by proper extrapolation with Taylor impact tests. *Int. J. Impact Eng.* 91, 142–157. <https://doi.org/10.1016/j.ijimpeng.2016.01.004>.
- Piao, M.J., Huh, H., Lee, I., Park, L., 2017. Characterization of hardening behaviors of 4130 Steel, OFHC Copper, Ti6Al4V alloy considering ultra-high strain rates and high temperatures. *Int. J. Mech. Sci.* 131–132, 1117–1129. <https://doi.org/10.1016/j.ijmecsci.2017.08.013>.
- Prasad, Y.V.R.K., Sasidhara, S., Gegele, H.L., Malas, J.C., 1997. Hot Working Guide: A Compendium of Processing Maps. ASM International, pp. 104–105.
- Rahmaan, T., Abedini, A., Butcher, C., Pathak, N., Worswick, M.J., 2017. Investigation into the shear stress, localization and fracture behaviour of DP600 and AA5182-O sheet metal alloys under elevated strain rates. *Int. J. Impact Eng.* 108, 303–321. <https://doi.org/10.1016/j.ijimpeng.2017.04.006>.
- Rahmaan, T., Bardelcik, A., Imbert, J., Butcher, C., Worswick, M.J., 2016. Effect of strain rate on flow stress and anisotropy of DP600, TRIP780, and AA5182-O sheet metal alloys. *Int. J. Impact Eng.* 88, 72–90. <https://doi.org/10.1016/j.ijimpeng.2015.09.006>.
- Ramazani, A., Bruehl, S., Abbasi, M., Bleck, W., Prahl, U., 2016. The effect of bake-hardening parameters on the mechanical properties of dual-phase steels. *Steel Res. Int.* 87 (11), 1559–1565.
- Ramazani, A., Bruehl, S., Gerber, T., Bleck, W., Prahl, U., 2014. Quantification of bake hardening effect in DP600 and TRIP700 steels. *Mater. Des.* 57, 479–486. <https://doi.org/10.1016/j.matdes.2014.01.001>.
- Riedmiller, M., Braun, H., 1993. A direct adaptive method for faster backpropagation learning: the RPROP algorithm. In: IEEE Int. Conf. Neural Networks - Conf. Proc. 1993-Janua, pp. 586–591. <https://doi.org/10.1109/ICNN.1993.298623>.
- Roth, C.C., Gary, G., Mohr, D., 2015. Compact SHPB system for intermediate and high strain rate plasticity and fracture testing of sheet metal. *Exp. Mech.* 55, 1803–1811. <https://doi.org/10.1007/s11340-015-0061-x>.
- Roth, C.C., Mohr, D., 2014. Effect of strain rate on ductile fracture initiation in advanced high strength steel sheets: experiments and modeling. *Int. J. Plast.* 56, 19–44. <https://doi.org/10.1016/J.IJPLAS.2014.01.003>.
- Roth, C.C., Mohr, D., 2016. Ductile fracture experiments with locally proportional loading histories. *Int. J. Plast.* 79, 328–354. <https://doi.org/10.1016/j.ijplas.2015.08.004>.
- Rumelhart, D.E., Hinton, G.E., Williams, R.J., 1986. Learning representations by back-propagating errors. *Nature* 323, 533–536. <https://doi.org/10.1038/323533a0>.
- Rusinek, A., Zaera, R., Klepaczko, J.R., 2007. Constitutive relations in 3-D for a wide range of strain rates and temperatures - application to mild steels. *Int. J. Solids Struct.* 44, 5611–5634. <https://doi.org/10.1016/j.ijsolstr.2007.01.015>.
- Sjöberg, T., Kajberg, J., Oldenburg, M., 2018. Calibration and validation of three fracture criteria for alloy 718 subjected to high strain rates and elevated temperatures. *Eur. J. Mech. A Solid.* 71, 34–50. <https://doi.org/10.1016/j.euromechsol.2018.03.010>.
- Sung, J.H., Kim, J.H., Wagoner, R.H., 2010. A plastic constitutive equation incorporating strain, strain-rate, and temperature. *Int. J. Plast.* 26, 1746–1771. <https://doi.org/10.1016/j.ijplas.2010.02.005>.
- Swift, H.W., 1952. Plastic instability under plane stress. *J. Mech. Phys. Solid.* 1, 1–18. [https://doi.org/10.1016/0022-5096\(52\)90002-1](https://doi.org/10.1016/0022-5096(52)90002-1).
- Tamura, S., Tateishi, M., 1997. Capabilities of a four-layered feedforward neural network: four layers versus three. *IEEE Trans. Neural Netw.* 8, 251–255. <https://doi.org/10.1109/72.557662>.
- Tancogne-Dejean, T., et al., 2016. Probabilistic fracture of Ti-6Al-4V made through additive layer manufacturing. *Int. J. Plast.* 78.
- Voce, E., 1948. The relationship between stress and strain for homogeneous deformation. *J. Inst. Met.* 74, 537–562.
- Voyiadjis, G.Z., Abed, F.H., 2005. Microstructural based models for bcc and fcc metals with temperature and strain rate dependency. *Mech. Mater.* 37, 355–378. <https://doi.org/10.1016/j.mechmat.2004.02.003>.
- Wang, J., Guo, W.-G., Li, P., Zhou, P., 2017a. Modified Johnson-Cook description of wide temperature and strain rate measurements made on a nickel-base superalloy. *Mater. A. T. High. Temp.* 34, 157–165. <https://doi.org/10.1080/09603409.2016.1252164>.
- Wang, P., Qu, S., 2018. Analysis of ductile fracture by extended unified strength theory. *Int. J. Plast.* 104, 196–213. (December 2017) Available at: <https://doi.org/10.1016/j.ijplas.2018.02.011>.
- Wang, W., Ma, Y., Yang, M., Jiang, P., Yuan, F., Wu, X., 2017b. Strain rate effect on tensile behavior for a high specific strength steel: from quasi-static to intermediate

- strain rates. *Metals* 8, 11. <https://doi.org/10.3390/met8010011>.
- Wilson, D.R., Martinez, T.R., 2003. The general inefficiency of batch training for gradient descent learning. *Neural Network*. 16, 1429–1451. [https://doi.org/10.1016/S0893-6080\(03\)00138-2](https://doi.org/10.1016/S0893-6080(03)00138-2).
- Xiao, X., Mu, Z., Pan, H., Lou, Y., 2018. Effect of the Lode parameter in predicting shear cracking of 2024-T351 aluminum alloy Taylor rods. *Int. J. Impact Eng.* 120, 185–201. <https://doi.org/10.1016/j.ijimpeng.2018.06.008>.
- Yan, S., et al., 2016. A unified model for coupling constitutive behavior and micro-defects evolution of aluminum alloys under high-strain-rate deformation. *Int. J. Plast.* 85, 203–229. Available at: <https://doi.org/10.1016/j.ijplas.2016.07.011>.
- Zerilli, F.J., Armstrong, R.W., 1987. Dislocation-mechanics-based constitutive relations for material dynamics calculations. *J. Appl. Phys.* 61, 1816–1825. <https://doi.org/10.1063/1.338024>.